Available online at www.sciencedirect.com

ScienceDirect

Geochimica et Cosmochimica Acta 122 (2013) 363–397

Geochimica et Cosmochimica Acta

www.elsevier.com/locate/gca

Geochemical provincialism in the Iceland plume ☆

Oliver Shorttle *, John Maclennan, Alexander M. Piotrowski

Department of Earth Sciences, University of Cambridge, Downing Street, Cambridge CB2 3EQ, UK

Received 11 November 2012; accepted in revised form 25 August 2013; available online 5 September 2013

Abstract

We present new Pb–Sr–Nd isotope, major and trace element data for a suite of basalts from central Iceland. We combine this new data with existing sample sets and interrogate it using spatial statistical methods. On the ~ 100 km scale of a volcanic zone we find strong correlation between the three isotope systems. However, on greater length scales we identify two types of spatial structure, both of which are most strongly observed in the Pb isotopes. Firstly, the mean Pb-isotopic composition of basalts becomes progressively less radiogenic from south to north Iceland, with our central Iceland dataset falling at intermediate compositions. Secondly, there is a shift in the pseudo-binary mixing array that samples fall along as the neovolcanic zones are stepped through south to north, both in Pb–Pb, and Pb–Sr/Nd isotope space. The Pb isotope systematics of Icelandic basalts therefore appear to be decoupled from those of Sr and Nd isotopes on length scales > 140 km. Only within individual neovolcanic zones are there coherent relationships between the Pb, Sr and Nd isotopic compositions of basalts. The spatial structure uniquely recorded by Pb isotopes complements observations from previous authors that Pb isotope dynamics are fundamentally distinct from other isotope systems.

Iceland lies at the centre of a geochemical transition that occurs in the North Atlantic mantle. Our analysis shows that this shift occurs progressively from the southwest to north east of the island. However, geochemical spatial structure on Iceland does not map simply into adjacent ridges. We find that at length scales > 200 km partial melting of the plume head during outflow can explain some of the transition to unradiogenic Pb isotopic compositions north of Iceland. However, the shift in binary mixing arrays to sources with higher time integrated Th/U, requires the North Atlantic mantle to be highly provincial in its Pb isotopic composition.

The spatial trends that we observe on Iceland are similar to those seen on Hawaii between the Loa and Kea volcanic chains, which also show shifts in mean Pb isotopic composition and binary mixing array. However, on Iceland we are able to see that, rather than representing dichotomous compositional domains on either side of the island, the change in mean composition and mixing array occurs continuously. Geochemical structure only shows segmentation on the scale of a neovolcanic zone. Discrete arrays in isotopic space on the scale of volcanic systems may develop in response to mixing in the melt transport and storage system and require neither the shallow nor the deep mantle to exhibit sharp (< 100 km) lateral contrasts in composition.

1. INTRODUCTION

The compositional structure of Earth's mantle contains a record of its differentiation, from a molten ball to a chemically stratified and tectonically active planet. Compositional structure has been created by partial melting, recycling, and convection all of which evolve and redistribute material throughout the Earth system. The present day

* Corresponding author. Tel.: +44 1223333474.

E-mail addresses: os258@cam.ac.uk (O. Shorttle), jcm1004@cam.ac.uk (J. Maclennan), amp58@cam.ac.uk (A.M. Piotrowski).

0016-7037/$ - see front matter © 2013 The Authors. Published by Elsevier Ltd. All rights reserved.
http://dx.doi.org/10.1016/j.gca.2013.08.032

spatial distribution of chemical domains acts not only as a historical record of this differentiation, but provides a clue as to how dynamic processes on Earth operate. To observe the geochemical structure of the mantle we often use mid-ocean ridges and ocean island volcanoes to act as the sampling mechanism. From the chemistry of basalts generated in these settings the state of convection in the Earth has been inferred (Allègre, 1982), and hemispherical compositional structure identified (Dupré and Allègre, 1983; Hart, 1984; Iwamori and Nakamura, 2012).

As the abundance of high-precision isotope analyses has increased, spatial structure on smaller scales has been resolved. At Hawaii and a number of Pacific ocean islands, isotopic observations have been used to infer bilateral asymmetry in their respective plume conduits, tracking back through the volcanic chains for millions of years (Abouchami et al., 2005; Tanaka et al., 2008; Huang et al., 2011). It has been suggested that the bilateral asymmetry observed in the Hawaiian plume is the result of a lateral compositional gradient at the core–mantle boundary being advected into the shallow mantle (Weis et al., 2011). If the hypothesis of Weis et al. (2011) is correct, lateral compositional variations in mantle plumes provide a powerful tool for probing the chemistry and structure of the deep Earth. In contrast, Ballmer et al. (2011) have put forward a model in which topography at the base of the lithosphere causes asymmetric melting of plume material, generating bilateral asymmetry from a uniformly-heterogeneous source (i.e. a source where the wavelength of compositional variability is much less than the size of the melt region). The debate is whether source or process generates spatial structure in geochemistry. Being able to separate these mechanisms is essential if we are to identify the compositional structure of the mantle and its significance for Earth's evolution.

Most existing studies inferring geochemical spatial structure have dealt qualitatively with the spatial information, using it to group samples in isotope–isotope space (Peate et al., 2010; Huang et al., 2011; Weis et al., 2011). Once groups have been defined datasets are interrogated for differences in mean compositions and binary mixing arrays using a combination of graphical and statistical methods (e.g. the F-test used by Abouchami et al. (2005)). With the above method the spatial analysis is in effect performed at the data grouping stage, and subsequent statistical tests can only corroborate the initial decision about how to subdivide the samples. Solely using spatial information to represent group membership discards a richness of spatial information that could otherwise be extracted from a dataset. A priori assumptions about how to group data also allows for observer bias to predetermine the spatial outcome. The practicalities of graphing and statistically testing groups of data means there is a risk that false spatial segmentation will be imposed on a dataset. More fundamentally, separation of the data into discrete groups is at odds with the increasing evidence of pervasive small-scale heterogeneity being continuously created and destroyed at ridges and subduction zones: both statistical modelling and melt inclusion studies predict ubiquitous 100 m–100 km sized heterogeneities in the mantle (Allègre et al., 1984; Kellogg and Turcotte, 1987, 1990; Saal et al., 1998; Meibom and Anderson, 2003; Kobayashi et al., 2004; Agranier et al., 2005; Meyzen et al., 2007; Maclennan, 2008a). If inferences about the scale and distribution of mantle heterogeneity are to be tested, locational information needs to be explicitly incorporated into the analysis of geochemical data. By considering sample location, information on the spatial structure of geochemistry will switch from being an input to the data analysis to a result of it—in this way can we place quantitative constraints on the compositional structure of the upper mantle.

In this study we focus on the Iceland mantle plume and use basalt chemistry from subaerial eruptions and submarine basalts to resolve the plume's spatial geochemical structure. Iceland represents a unique opportunity to explore the chemical structure of the mantle: the superposition of a spreading ridge and mantle plume creates nearly spatially continuous volcanic activity on Iceland, whilst the Mid-Atlantic Ridge (MAR) acts as a linear sampler of the outflowing plume head over more than 1000 km. The spatial scale of access to the mantle under and around Iceland contrasts with most intraplate volcanoes, where sampling is focused at a small number of volcanic centres, severely limiting the spatial information obtainable (Fig. 1).

The presence of isotopic spatial structure within Iceland has been both suggested and refuted in the literature. A provincialism in the isotopic composition of measured basalts on Iceland was noticed early on from a limited sample set spanning a wide age range (Welke et al., 1968). With subsequent targeted studies of the neovolcanic zones, intrinsic mantle spatial structure was rejected in favour of a model where magma type (tholeiitic vs. alkaline basalt) was the most important control on isotopic composition (Hémond et al., 1988; Chauvel and Hémond, 2000). From a high-precision set of Pb isotope analyses, Thirlwall et al. (2004) found no relationship between location and Sr or Nd isotopic composition, but for Pb isotopes noted the significance of location particularly for the flank zones

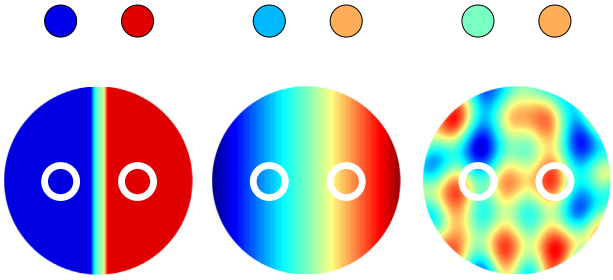

Fig. 1. Cartoon illustrating the limited information on mantle compositional structure accessible by a dual volcanic chain. The large circles represent a horizontal cross section through a plume conduit, coloured red–blue according to its composition. The chemical structure of the plume is sampled by two 'volcanoes' positioned at the small white circles, with the average composition of the mantle they sample shown in the two smaller filled circles at the top of each plot. Although very simple, this cartoon illustrates that two point samples of the mantle do not uniquely constrain spatial structure. In each case, the volcanoes produce dichotomous basalt compositions irrespective of the underlying structure.

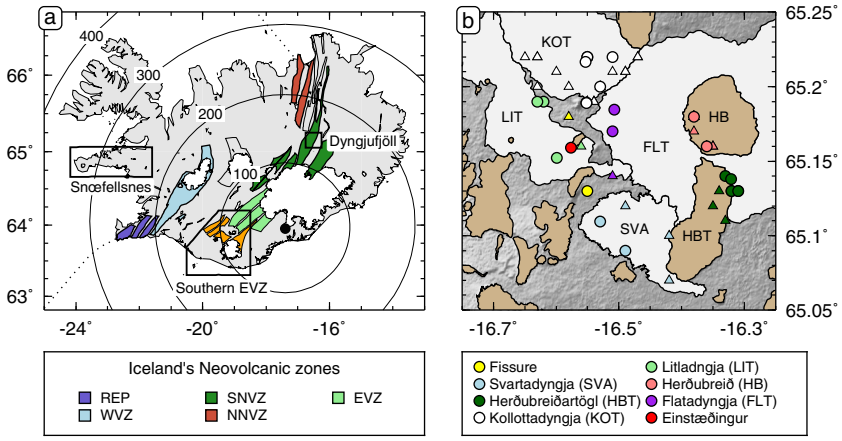

Fig. 2. (a) Map of Iceland showing its neovolcanic zones, the flank zone Snæfellsnes, the propagating rift of the southern Eastern Volcanic Zone (EVZ), and the sample area of this study, Dyngjufjöll. Neovolcanic zones used in grouping the data for the first phase of statistical analysis are coloured and their names given in the legend. Submarine ridges are marked on as dotted lines. The map has radial contours 100 km apart from an initial point source in south eastern Iceland (Shorttle et al., 2010). (b) Detailed map of the Dyngjufjöll region of central Iceland, the boundaries of postglacial eruptions (< 12 ka) are coloured white and glacial eruptions (12–80 ka) coloured brown. Sample localities and eruption names are marked on the map, circles represent samples from which we have made new isotopic analyses and triangles are samples from which we have major and trace element data from Maclennan et al. (2001). Flow boundaries from Hartley (2012).

(the regions of off-axis volcanism on Iceland, Fig. 2). With an expanded dataset, Peate et al. (2010) observed offsets in Pb isotope array between the Northern Northern Volcanic Zone (NNVZ), the south of the Eastern Volcanic Zone (sEVZ) and the Western Volcanic Zone/Reykjanes Peninsula (WVZ/REP).

On a regional scale, basalts dredged from the MAR have been used to identify separate geochemical domains in the North Atlantic mantle. Blichert-Toft et al. (2005) used Pb isotopes to distinguish the Reykjanes, Kolbeinsey and Mohns and Knipovich ridges from one another, each erupting basalts with a characteristic Pb isotope composition. A high Th/U component was inferred to be present north of Iceland in order to explain the offset of Pb isotopic arrays to high $^{208}Pb/^{204}Pb$. Hf isotopes have proved important in identifying unusually depleted (or high Lu/Hf) mantle domains, which have been inferred both as an intrinsic component of the plume itself (Kempton et al., 2000; Fitton et al., 2003) and as part of the geochemical transition occurring north of the Jan Mayen platform (Blichert-Toft et al., 2005). With hot plume material dispersing over several thousand kilometres around Iceland (Jones et al., 2002), it is important to try and link those observations made on Iceland near the plume's centre, with those made along adjacent ridges.

Our method in this contribution is fivefold. (1) We produce new Pb, Sr, Nd isotopic analyses for a central Iceland sample set, located in a key location to resolve spatial changes in geochemical composition. (2) We apply a conventional statistical analysis to the geochemical data from Iceland, grouping the data by neovolcanic zone to assess differences between the assumed geochemical provinces. We progress from univariate comparisons between zones to a bivariate analysis, which compares the structures of isotope–isotope arrays. (3) The statistical analysis is moved to the spatial domain, explicitly incorporating geographical location when calculating statistical parameters. Crucially, the data are not grouped by zone and the statistics used are sensitive to short length scale variability. (4) We develop cumulative chi-squared plots as means of representing diverse spatial parameters, in order to extract information on the length scale of geochemical provincialism on Iceland and test its significance against random spatial distributions. (5) Lastly, the spatial structure on Iceland is placed in context with the adjacent ridges. We show that the univariate and bivariate parameters mapped on Iceland are equivalent to the Pb-isotope principal components that have been used to define mantle chemical structure in the north Atlantic (Blichert-Toft et al., 2005).

Analysing geochemical data both with and without explicit locational information shows the advantages of a spatial analysis for extracting quantitative information on geochemical spatial structure. We find that Pb isotopic composition and Pb isotope array structure are strong functions of geographic location on Iceland. The Pb isotopes are decoupled from Sr and Nd isotopes on length scales > 140 km; at sample–sample distances greater than this, basalts will tend to have systematically different Pb isotopic compositions, but on average the same Sr and Nd isotopic composition.

The methods and discussion in this paper have broad application to the inference of geochemical spatial structure from basalt geochemistry, and in particular the identification of bilateral compositional asymmetry in plume conduits.

2. SAMPLES AND METHODS

To provide the resolution required to resolve spatial structure in Iceland's geochemistry, we combine existing high-precision isotopic data with our own Pb–Nd–Sr analyses on a sample set from central Iceland. Our data fill in a

gap in the sample coverage of Iceland and, together with published data, provide an average sample density for the ~500 km of neovolcanic zones of ~1 sample per 4 km (for samples with joint Pb, Sr and Nd isotopic analyses). For comparison, the Reykjanes Ridge, an unusually well studied section of mid-ocean ridge, has been sampled at a level of ~1 *sample per* 14 km. As a result of this contrast in sampling density, spatial structure on a < 100 km scale, which will be resolvable on Iceland, will be almost impossible to see along the submarine ridges.

In this section our sampling and analysis methods are discussed, followed by details of how additional data were selected from the literature to produce a composite dataset.

2.1. Sample collection

The Dyngjufjöll area lies at the southern end of Iceland's northern neovolcanic zone (Fig. 2a), and is often associated with the Askja fissure system. Samples were collected from a region bounded by the Askja volcanic centre to the south and the Fremrinámar volcanic system in the north west. All samples are from volcanic structures of glacial and post-glacial age (all < 80 ka); their locations are shown in Fig. 2b with details given in Table 1. Four post-glacial lava shields have been sampled for scoria and whole-rock. One tuya and two hyaloclastite ridges have been sampled for a range of whole-rock and glassy pillow material. Ages of subglacial units are poorly constrained, but a He exposure age from the top of the Herðubreið tuya gave an age of 10.5 ± 0.6 ka (Licciardi et al., 2007), suggesting that many of these subglacial structures could have formed at the very end of the last glacial. The region is also cut by many fissure eruptions, of which we have analysed whole-rock material from one in the south.

2.2. Analytical techniques

Data in this study supplement the major and trace element data of Maclennan et al. (2001) with new Pb, Sr and Nd isotopic analyses for 16 Dyngjufjöll lavas, and represent a new set of comprehensive major, trace and isotopic analyses for a further 8 samples.

Major element analyses and a subset of the trace elements (Nb, Zr, Y, Sr, Zn, Cu, Ni and Cr) were obtained by XRF at the University of Edinburgh following the method of Fitton et al. (1998). Fresh, clean sample was crushed in a steel jaw crusher and then ground to a powder in agate at the Department of Earth Sciences, University of Cambridge, with the subsequent glass disk and pressed powder pellet stages occurring at the University of Edinburgh. Remaining trace elements were obtained by ICP-MS (Perkin Elmer Elan DRCII) at the Department of Earth Sciences, University of Cambridge. From each powder, 0.1 g was dissolved in a sealed beaker using a mixture of 1 ml 16 N QD HNO_3 and 4 ml 48% HF at 120 °C for 24 h. Once the samples were completely dissolved the HF was progressively evaporated off; at each stage before the sample completely dried down 1 ml 16 N QD HNO_3 was added. 1 *ml* 16 *N QD* HNO_3 was added three times before the samples were picked up in 2.5 ml 16 N QD HNO_3 and diluted to 3.5% HNO_3 for running on solution mode ICP-MS. As well as the samples, powders from USGS standards BCR-2 and BIR1 were taken through the dissolution process to ensure the procedure could reproduce reference values.

Pb, Sr and Nd isotopic analyses were carried out in three sessions at the Department of Earth Sciences, University of Cambridge, in February 2010, May 2010 and October 2011. Samples were hand-crushed, from which 0.3 g of the freshest rock chips and glass was picked under a binocular microscope. In the clean labs, these chips were then rinsed in MQ-water (18.2 MΩ cm), washed in an ultrasonic bath for 20 min, and given a final MQ-water rinse to remove any adhered material. As a further precaution against contamination, samples were acid-leached. A two-stage leach was used for rock chips, whilst glassy material was only subjected to the second leaching step. Firstly, samples were leached in 1 ml 6 N HCl heated to 150 °C for 1 h. The supernatant was then pipetted off and replaced with a fresh 1 ml 6 N HCl. In the second leaching step, samples were ultrasonicated for 20 min and then placed on the hotplate at 150 °C for 30 min. Remaining acid was then rinsed off with MQ-water. Mass loss during the cleaning process was ~10%. Samples were then dissolved in a mixture of 1.5 ml 48% HF and 3 ml 16 N QD HNO_3, left on a hotplate at 110 °C for 48 h or until all material had dissolved. After drying down, samples were successively picked up and dried down in 16 N QD HNO_3 and 6 N HCl to remove fluoride precipitates. The first stage of chromatography separated Pb using Eichrom AG1-X8 resin (100–200 μm mesh) in

Table 1
Eruptions sampled in the Dyngjufjöll area of central Iceland for this study.

Eruption	Type	Age (ka)	Volume (km^3)
Einstæðingur	Hyaloclastite ridge	≥ 10.5	0.03
Herðubreiðartögl	Hyaloclastite ridge	> 10.5	7.6
Herðubreið	Tuya	10.5 ± 0.6[b]	10
Kollóttadyngja	Lava shield	> 4500[b]	17
Svartadyngja	Lava shield	> 4500[b]	1
Fissure	Fissure lava	3500–4500[b]	0.3
Flatadyngja	Lava shield	3500–4500[b]	2.6
Litladyngja	Lava shield	2900–3500[b]	1.7

[a] Age from Licciardi et al. (2007).
[b] Age from Sigvaldason et al. (1992).

Table 2
Isotopic data for Dyngjuföll samples and USGS standards.

Sample	Material[a]	Location	Long. (°E)	Lat. (°N)	$^{87}Sr/^{86}Sr$	2σ[b]	$^{143}Nd/^{144}Nd$	2σ	$^{206}Pb/^{204}Pb$	2σ	$^{207}Pb/^{204}Pb$	2σ	$^{208}Pb/^{204}Pb$	2σ
BOL09-1	pg	Einstæðingur	−16.58	65.16	0.703290	6	0.513028	13	18.377	2	15.467	1	38.122	5
FL01	w	Flatadyngja	−16.31	65.13	0.703299	11	0.513027	11	18.357	2	15.474	2	38.122	5
FL04	w	Flatadyngja	−16.51	65.17	0.703196	10	0.513050	9	18.462	2	15.464	2	38.147	6
					0.703187	11	0.513051	9	18.465	2	15.466	2	38.152	6
FLT09-1	s	Flatadyngja	−16.51	65.18	0.703242	5	0.513048	13	18.460	2	15.463	1	38.157	5
HB02	w	Herðubreið	−16.38	65.18	0.703275	10	0.513029	19	18.381	2	15.478	2	38.160	6
HB09	w	Herðubreið	−16.36	65.16	0.703209	11	0.513052	19	18.356	2	15.473	2	38.111	6
HBT01	w	Herðubreiðartögl	−16.32	65.13	0.703221	11	0.513066	11	18.308	2	15.461	3	38.014	7
HBT02	w	Herðubreiðartögl	−16.32	65.13	0.703101	11	0.513090	19	18.294	1	15.461	2	37.993	4
					0.703108	10	0.513100	19	18.288	1	15.452	2	37.971	4
HBT07	w	Herðubreiðartögl	−16.33	65.14	0.703268	10	0.513044	19	18.346	2	15.477	2	38.106	6
HBT08	w	Herðubreiðartögl	−16.31	65.13	0.703102	5	0.513098	10	18.289	2	15.442	1	37.945	5
HBT10-1	pg	Herðubreiðartögl	−16.32	65.14	0.703127	5	0.513080	13	18.278	2	15.442	1	37.937	5
KO01	w	Kollottadyngja	−16.53	65.20	0.703295	10	0.513016	19	18.379	2	15.483	2	38.175	6
KO18	w	Kollottadyngja	−16.51	65.22	0.703280	10	0.513026	11	18.347	2	15.477	3	38.126	7
KO20	w	Kollottadyngja	−16.55	65.22	0.703267	5	0.513034	10	18.329	2	15.473	1	38.109	5
KO24	w	Kollottadyngja	−16.55	65.22	0.703266	10	0.513030	23	18.326	2	15.474	2	38.108	6
					0.703259	10	0.513036	23	18.320	2	15.469	2	38.088	6
KOT09-1	s	Kollottadyngja	−16.55	65.19	0.703328	5	0.513033	13	18.466	2	15.473	1	38.202	5
KOT09-2	w	Kollottadyngja	−16.55	65.19	0.703280	7	0.513040	10	18.402	2	15.473	1	38.141	5
KOT09-3	s	Kollottadyngja	−16.55	65.22	0.703262	5	0.513028	10	18.320	2	15.462	1	38.073	5
LI01	w	Litladyngja	−16.62	65.19	0.703295	5	0.513016	10	18.443	2	15.487	1	38.226	5
LI02	w	Litladyngja	−16.63	65.19	0.703345	11	0.513025	19	18.437	2	15.479	2	38.193	6
LIT09-1	w	Litladyngja	−16.60	65.15	0.703275	5	0.513026	13	18.418	2	15.467	1	38.147	5
RE02	w	Fissure	−16.55	65.13	0.703322	11	0.513019	19	18.430	2	15.484	2	38.178	6
SV03	w	Svartadyngja	−16.49	65.09	0.703256	10	0.513052	11	18.414	2	15.468	3	38.127	7
SVA09-1	s	Svartadyngja	−16.53	65.11	0.703252	5	0.513034	13	18.412	2	15.468	1	38.120	5
BCR-2									18.754	2	15.622	2	38.730	5
									18.752	2	15.621	2	38.715	5
BCR-2[c]	Woodhead and Hergt (2000), $n = 4$								18.753	21	15.620	7	38.713	42
BCR-2	Collerson et al. (2002), $n = 3$								18.757	12	15.621	9	38.720	18
BCR-2	Baker et al. (2004), $n = 8$								18.765	11	15.625	5	38.749	22
BIR-1									18.850	2	15.657	2	38.492	5
									18.846	2	15.654	2	38.481	5
BIR-1	Baker et al. (2004), $n = 3$								18.851	5	15.659	1	38.498	6
BIR-1	Chauvel et al. (2011)								18.841	5	15.658	4	38.487	13

[a] Type of sample material, w = whole − rock, pg = pillowglass, s = scoria.
[b] For $^{87}Sr/^{86}Sr$ analyses 2σ corresponds to the internal precision. For Pb and Nd analyses, 2σ represents the external reproducibility, calculated from the bracketing standards run during the analytical session (NIST SRM-981 and La Jolla respectively).
[c] Reported USGS reference material Pb isotopic ratios are corrected for normalisation to different values of NIST SRM-981. Errors are reported as 2σ and where 'n' is given are calculated from repeated runs of the material.

100 µl Teflon columns. After initial separation of Pb, the cuts from the May 2010 and October 2011 sessions were passed through the columns a second time to reduce the cation load in the final Pb fraction (Barling and Weis, 2008). The rare earth element (REE) fraction was separated using Eichrom TRUspec® resin (100–150 µm mesh), and the Nd fraction using LNspec® resin (50–100 µm mesh) on volumetrically calibrated Teflon columns. The remainder of the sample after the TRUspec® stage went on to have Sr separated out using volumetrically calibrated columns with filtered Dowex® 50 W X 8-400 resin. Procedural blanks for Pb were between 30–90 pg, for Nd 100–200 pg and for Sr 94–470 pg.

The Pb and Nd isotopic compositions of samples were measured using a Nu Plasma multi-collector inductively-coupled plasma mass-spectrometer (MC-ICP-MS). Samples were taken up in 0.3 N QD HNO_3 and introduced into the plasma using a Nu instruments DSN100 desolvating nebulizer. All measurements were made in static mode. For Pb isotopic analyses samples were spiked each session with fresh Tl solution as an internal standard at a Pb/Tl ratio of 2 (Rehkämper and Mezger, 2000). Samples were run between 40 and 50 ppb Pb. The Hg beam was monitored at mass 202, and a correction for interference of ^{204}Hg with ^{204}Pb was made using natural $^{204}Hg/^{202}Hg = 0.229$ corrected for mass fractionation (Zadnik et al., 1989). During each run NIST SRM-981 was run as a bracketing standard. For Nd isotope analysis the JNdi-1 neodymium isotope standard of Tanaka et al. (2000) ($^{143}Nd/^{144}Nd = 0.512115$) was used to bracket each sample. The Sm beam was monitored on mass 147, and throughout analytical sessions was $> 10^{-4}$ times less than the ^{144}Nd beam. Samples and standards were concentration matched at 100 ppb Nd.

There have been a number of studies discussing corrections for instrumental mass fractionation e.g. Rehkämper

and Halliday (1998), White et al. (2000), Vance and Thirlwall (2002), Albarède et al. (2004), Woodhead (2002), Kamenov et al. (2004), with a variety of resulting methods. An important result is the efficacy of the exponential law in removing the effect of mass fractionation (White et al., 2000), and we apply this correction law to both Nd and Pb isotopic data. As Pb isotopes lack a natural stable isotope pair to track instrumental mass fractionation we have spiked our samples with Tl before analysis. It is then necessary to assume or determine the relationship between the fractionation factors of Pb and Tl (f_{Pb} and f_{Tl} respectively). It has been demonstrated by White et al. (2000) that in general $f_{Pb} \neq f_{Tl}$ and these authors suggest empirically determining the relationship between f_{Tl} and f_{Pb} for each analytical session. However, we found that to obtain a precise relationship between f_{Tl} and f_{Pb} required changing the conditions of the instrument such that the magnitude of mass fractionation was not stable analysis to analysis—these conditions are contrary to an ideal analysis setup, where the magnitude of mass bias is preferably very stable. For this reason we chose to apply the exponential law correction using $f_{Pb} = f_{Tl}$ and then apply a small linear correction for the offset of the bracketing standards from the reported NIST SRM-981 value of Galer and Abouchami (1998), Abouchami et al. (2000) ($^{208}Pb/^{204}Pb = 36.7219$, $^{207}Pb/^{204}Pb = 15.4963$, $^{206}Pb/^{204}Pb = 16.9405$). A constant $^{205}Tl/^{203}Tl = 2.3889$ was assumed. To ensure the similarity of the bracketing and standards and samples, and thus an effective bracketing correction, Pb–Tl concentrations were matched between the standard and the sample (Rehkämper and Mezger, 2000), and for the May 2010 and October 2011 sessions samples were passed twice through the cation exchange columns (Barling and Weis, 2008). The accuracy of our correction approach is demonstrated in Fig. A.1 and the associated discussion in the supporting material.

Nd isotopic analyses were corrected for instrumental mass fractionation using an exponential correction law to the natural $^{146}Nd/^{144}Nd = 0.7219$.

Sr isotopic analyses were performed on a VG Sector 54 thermal ionisation mass spectrometer at the Department of Earth Sciences, University of Cambridge. A dynamic triple collector algorithm was used following the method of Bickle et al. (2003) and values were normalised to a $^{86}Sr/^{88}Sr = 0.1194$ with an exponential law to correct for mass fractionation. Over the analytical period the NIST SRM-987 standard reproduced with a $^{87}Sr/^{86}Sr$ ratio of 0.710263 ± 0.000008 (1 sigma) and values here are reported with respect to a NIST SRM-987 $^{87}Sr/^{86}Sr$ ratio of 0.710248.

2.3. Selection of literature data

References for literature data combined with new data from this study are presented in Table B.7 of the supporting material. Below we outline the criteria employed in constructing the database.

2.3.1. Filters applied to data selection

To constrain spatial patterns of mantle heterogeneity it is necessary to control for time. A dataset of samples erupted in as short a time period as possible limits the effect mantle flow has in redistributing geochemical domains and provides a snapshot of mantle structure. To obtain a sufficiently large dataset we have included samples with eruption ages from within the last glacial cycle on Iceland (< 80 ka). Assuming an average solid upwelling velocity within the melt region of 10 mm/yr (half plate spreading), then over 80 kyr material will only have moved ~ 800 m. A potential complication is that beneath central Iceland upwelling velocities, at least at the base of the melt region, are likely to be an order of magnitude greater than plate spreading (Ito et al., 1999; Maclennan et al., 2001; Kokfelt et al., 2003; Koornneef et al., 2012a). Large amounts of material could therefore be fluxed through some parts of the melt region in even 80 kyr.

The isotopic compositions of Icelandic basalts should be minimally affected by interaction with the crust. With a young crustal age allowing for little radiogenic ingrowth, and a similar Pb content of young and old basalts (Kitigawa et al., 2008), crustal material should not exert a strong leverage on basalt Pb contents. Instead, the main consequence of crustal magma storage on isotopic composition is likely to be a decrease in geochemical variability via concurrent mixing and crystallisation (Maclennan, 2008b). There could be some influence of sea water on Sr isotopic compositions close to the coast if basalts assimilate large quantities of hydrothermally altered crust (Elderfield and Greaves, 1981). As a precaution we only include samples with ≥ 5 wt% MgO. Limiting the samples in this way should not affect results, as by 5 wt% MgO most mantle derived geochemical primary variability has been mixed out (Shorttle and Maclennan, 2011). Fig. 3 A consequence of filtering by MgO is that samples with no major element analyses are also excluded.

Whilst Sr and Nd isotopic analyses often show significant scatter because of their low signal to noise, they suffer less from the systematic errors associated with correcting for mass fractionation that can easily accompany a Pb isotope analysis. In general, Pb isotope analyses published before the year 2000 show a degree of scatter that has reduced subsequently; both as methods for correcting for mass fractionation have become more advanced e.g. Woodhead (2002) and as the importance of sample leaching has been realised e.g. Silva et al. (2009). As a result, all Pb isotopic analyses come from papers published after the year 2000. After the year 2000 analyses are excluded where they have been shown to be systematically in error. Although these rules for data inclusion may appear stringent, relatively few analyses are excluded in this way, and the subsequent results do not depend on excluding any particular dataset. For Sr and Nd isotopic data we have been more inclusive of existing data and this accounts for the larger number of Sr and Nd analyses in Table B.7. However, when statistics calculated from Pb isotopes are being compared to those for Sr and Nd, unless otherwise indicated, one set of samples with common Pb–Sr–Nd analyses are used.

We primarily consider samples from the neovolcanic zones (marked on Fig. 2), although data from Snæfellsnes and the southern Eastern Volcanic Zone are shown for reference in some sections. Focusing on the neovolcanic zones

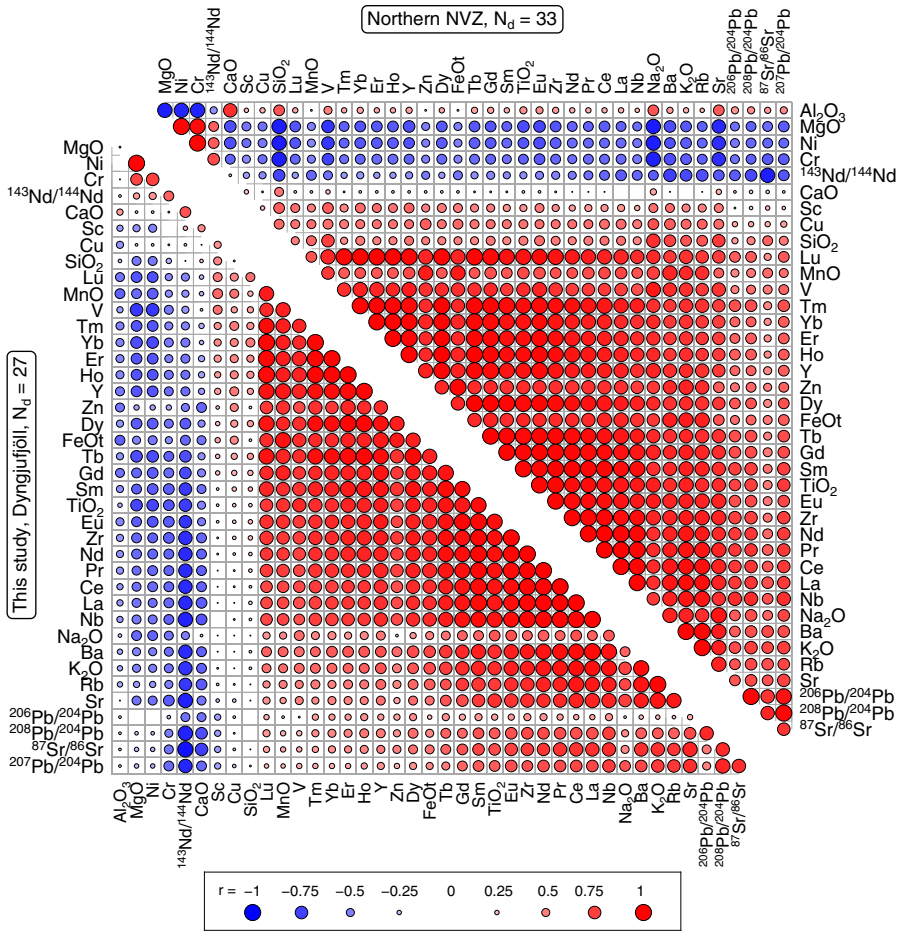

Fig. 3. The correlation matrix of data from the Dyngjufjöll area (this study, lower left matrix), compared with a compilation of data from the northern NVZ (data from Kempton et al., 2000; Stracke et al., 2003, upper right matrix). Points are coloured and scaled by the strength of correlation between the two elements with larger points indicating a stronger correlation, blue points a negative correlation and red points a positive correlation.

is necessary partly because of the previously mentioned data requirements, but also because the inclusion of flank zone eruptions will cause spatial signals to become dominated by the changing melt regime and melt transport processes away from the rift zones. Considering data from only the neovolcanic zones gives changes in the chemical structure of the plume head the best chance of being visible from the data.

One specific sample has been left out: RP103A from the Reykjanes Peninsula (REP) (Thirlwall et al., 2004). RP103A has a unique isotopic characteristic: high $^{87}Sr/^{86}Sr$, low ϵNd and an unusual Pb isotopic composition which gives it high ^{206}Pb normalised ratios (Thirlwall et al., 2004). Whilst RP103A may reflect a genuine component within the Icelandic mantle, its offset from mixing arrays defined by other samples in the same neovolcanic zone, and the lack of expression of its signature in other regions of Iceland, suggests that it is spatially restricted. More practically, RP103A's extreme isotopic composition will give it a large amount of leverage on any statistics calculated. To avoid undue control by RP103A on the results obtained it is not included in the subsequent statistical analysis.

2.3.2. Error data

The statistical schemes we apply take into consideration error in both the x and y coordinate and, where appropriate, the correlation coefficient of this error. As a result, only data for which it is possible to find some estimate of analytical uncertainty is included. For correlated error in Pb–Pb isotope space, correlation coefficients are calculated from Albarède et al. (2004) assuming that correlation is due to shot noise. It is important to incorporate consistent analytical error estimates into the database; however, published estimates of analytical uncertainty and styles of reporting vary widely. We adopt the external reproducibility of a standard, run in the same analytical session as the sample, as the preferred measure of uncertainty. It is the standard deviation (σ), as a measure of this external reproducibility, which we use in calculation of the statistics in this study.

2.3.3. Data normalisation

In establishing differences between datasets it is preferable to have all the data normalised to the same reference values of standards and natural compositions. However, it is not always clear which reference standards have been

used in producing published data. Other inter-lab biases could also exist, which cause datasets to be offset in isotope space from one another (e.g. uncorrected mass bias). Lab biases are a particularly acute problem when analyses from single labs dominate the available data for a region, as this could generate the false impression of spatial structure in geochemical observables. To account for all inter-lab effects, we adopt a Jackknifing routine to quantify the dependence of statistical parameters on the data from single labs. The algorithm followed is that each statistic is repeatedly recalculated, leaving out all the data from a given lab in a particular neovolcanic zone on each recalculation step. A population of values for a statistic is thereby obtained, equal in number to unique author-zone pairings, from which a mean and standard deviation of the statistic can be calculated.

3. RESULTS AND COMPARISON TO PUBLISHED DATA

3.1. Major and trace elements

The full Dyngjufjöll dataset, including the major and trace element analyses, can be found in the online electronic version of the manuscript. In Fig. 3 we present a graphical summary of the elemental and isotopic data we have collected, which shows the Dyngjufjöll ordered correlation matrix (bottom left triangular matrix), compared to data from Theistareykir (Stracke et al., 2003; Kempton et al., 2000) (upper right triangular matrix). The striking result of comparing Theistareykir and Dyngjufjöll is the similarity in the behaviour of element pairs between the two datasets. The basic systematic of strong positive correlations between the incompatible trace elements, and a negative correlation between the incompatible and compatible trace elements (Ni and Cr) is present in both. For the major elements the two datasets show some differences, most notably in Al_2O_3, which changes its behaviour from compatible (in the Dyngjufjöll dataset) to incompatible in the Theistareykir data. The most likely cause of differences between the two datasets' major element compositions is the effect of olivine accumulation in the Theistareykir samples—mean MgO = 11.3 wt% compared with a mean MgO of 8.8 wt% in Dyngjufjöll samples—and plagioclase accumulation in the Dyngjufjöll samples. The strong correlations between FeO and the incompatible elements hints at the convolution of depth and degree of melting with source lithology, in controlling the correlations between raw elemental concentrations (Stracke et al., 2003; Shorttle and Maclennan, 2011; Rudge et al., 2013).

3.2. Pb–Nd–Sr isotopes

The new Sr–Nd–Pb isotope data from this study are reported in Table 2. A test of the accuracy of the Tl spiking method for mass fractionation correction is possible by comparison between the USGS reference materials we ran and published analyses (Table 2). Our analyses of BCR-2 lie within error of the double spike TIMS values from Woodhead and Hergt (2000) and Tl corrected MC-ICP-MS data of Collerson et al. (2002), but are slightly lower than those of Baker et al. (2004). The lower concentration of Pb in BIR-1 compared with BCR-2 ($\sim$ 2 ppm vs. $\sim$ 10 ppm) makes BIR-1 a more stringent test of the method. Our BIR-1 values reported in Table 2 are within error of both the reported TIMS double spike values of Baker et al. (2004) and Tl corrected MC-ICP-MS values of Chauvel et al. (2011). It is therefore likely that the new data we report are free from substantial bias as a result of the Tl spiking method.

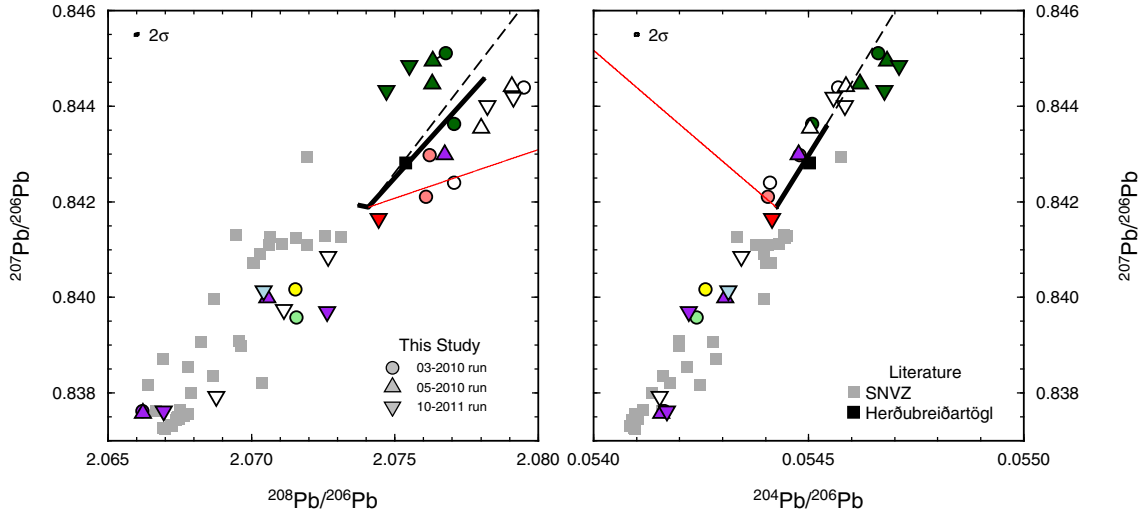

Fig. 4. This study's Pb isotope data compared to literature data from central Iceland. Symbols connected by a line represent repeat analyses. The first two principal component vectors for the data from this study are drawn as thick black lines, scaled by the relative proportion of the variance they explain (principal component 1, PC1, accounts for 94.3% of variance and PC2 5.6% and is as such barely visible in 46–76 space). The dashed black line is a vector towards the Broken Hill galena composition of Rudnick and Goldstein (1990). Thin red line marks the direction mass dependent fractionation. Error ellipses are the average for the data from this study. Literature data from Breddam et al. (2000), Kokfelt et al. (2006), Kuritani et al. (2011).

In the Fig. 4 plot of $^{207}Pb/^{206}Pb$ vs. $^{208}Pb/^{206}Pb$ the new data form a coherent array extending from the most radiogenic compositions, represented by Flatadyngja ($^{208}Pb/^{206}Pb = 2.0662$), to the unradiogenic basalts of Herðubreiðartögl ($^{208}Pb/^{206}Pb = 2.077$). Although Herðubreiðartögl is the only eruption sampled by both literature data and this study, there is general agreement between the datasets; with our new data extending the central Iceland array to slightly less radiogenic compositions. Principal component analysis performed on the new Dyngjufjöll Pb isotopes (normalised to ^{206}Pb), indicates that 99.9% of the variance is explained by two principal components (PC1 and PC2, Fig. 4). Two significant principal components means that in three dimensional Pb isotope space the data resolve almost perfectly into a plane, with a minimum of three mixing endmembers required to explain all the variability.

Within the Dyngjufjöll region it is the data from Herðubreiðartögl that deviate most notably from a single binary mixing array and that generates the need for a second significant principal component. Four out of the five samples from Herðubreiðartögl possess low $^{208}Pb/^{206}Pb$ at a given $^{207}Pb/^{206}Pb$, or described using ^{204}Pb: low $^{208}Pb/^{204}Pb$ at a given $^{207}Pb/^{204}Pb$ and $^{206}Pb/^{204}Pb$ (Fig. 4). In $^{207}Pb/^{206}Pb$ vs. $^{204}Pb/^{206}Pb$ space PC2 is insignificant and 99% of the variability is accounted for by binary mixing along PC1. The second principal component only becomes important when $^{208}Pb/^{206}Pb$ is included, where PC2 mainly moves data to higher or lower $^{208}Pb/^{206}Pb$ at a given $^{207}Pb/^{206}Pb$. Neither contamination from anthropogenic Pb nor inadequate mass fractionation correction is likely to account for the offset of the Herðubreiðartögl data. Fig. 4 plots both the directions of mass dependent fractionation and the vector towards Broken Hill galena, a probable source of common Pb. However, the vector of anthropogenic contamination is almost perpendicular to PC2 and procedural blanks were insignificant given the amount of sample analysed. Uncorrected mass fractionation in the Herðubreiðartögl analyses is closer to moving data in the direction of PC2 (Fig. 4 red line). Given our analysis method, the most probable cause of inadequate correction for mass fractionation occurring in the MC-ICP-MS is non-spectral matrix effects leading to differential fractionation between Pb and Tl (Barling and Weis, 2008). One argument against non-spectral matrix effects being important is the similarity of our BCR-2 and BIR-1 values with published results (Woodhead and Hergt, 2000; Baker et al., 2004; Chauvel et al., 2011). In addition to this, the observed behaviour of sample HBT02 between the February and May 2010 analytical sessions is inconsistent with a role of matrix in determining Pb isotopic composition. Fig. 4 shows that the repeat of HBT02 in the May 2010 analytical session, by which point the chemistry had been modified to incorporate two passes through the Pb columns, plots further away from the main data array—opposite to what would be predicted if the initial offset of HBT02 was to be attributed to the presence of sample matrix. Relatively low $^{208}Pb/^{206}Pb$ at a given $^{207}Pb/^{206}Pb$ is thus a real feature of some basalts in the Dyngjufjöll region.

4. EVIDENCE FOR A REGIONAL ISOTOPIC COMPOSITION OF BASALTS

Variability in the isotopic composition of basalts is the key observation indicating that the mantle is compositionally heterogeneous. From studying olivine-hosted melt inclusions on Iceland we know that extreme isotopic variability exists within single melt regions (Maclennan, 2008a)—implying that the mantle is heterogeneous on length scales less than $\sim$ 100 km. However, there is also evidence that superimposed on this local variability are long wavelength changes in source, which give distinctive isotopic signatures to basalts erupted in different areas (Peate et al., 2010). Here we test the observation that Iceland's neovolcanic zones possess distinct isotopic compositions.

We first group the geochemical data by the neovolcanic zones identified in Fig. 2a. To compare the means and shapes of the distributions we construct kernel density estimates for each zone, and test the normality of the data using quantile–quantile (qq) plots (Fig. 5; more familiar isotope–isotope cross-plots are shown in Figs. 6 and 7 and discussed subsequently). The kernel density estimates can be thought of as smoothed histogram representations of the data (Rudge, 2008). The moments of each distribution are quantitatively recorded and discussed in C of the supporting material.

A striking feature of Fig. 5 is that the Pb isotopic composition of basalts from the NNVZ (left column of Fig. 5) are consistently less radiogenic than basalts from either central or northern Iceland (central and right-hand columns of Fig. 5 respectively). Basalts from south west Iceland are the most radiogenic, whilst central Iceland basalts have Pb isotopic compositions intermediate between the other two zones. In the Sr isotope kernel density plots the central Iceland data are displaced to slightly more radiogenic values than the south west and NNVZ data; however, the Nd isotopic composition of all neovolcanic zones are similar.

It is possible to formally assess whether the zones have different isotopic compositions using a Mann–Whitney test. The Mann–Whitney statistic tests for whether one of two sets of independent observations has a systematic shift with respect to the other. Table 3 reports the results of testing each neovolcanic zone's distribution against the two others using the Mann–Whitney test for Sr, Nd, and Pb isotopes. Of all the comparisons, only the Pb isotopes show consistent differences between neovolcanic zones at greater than 95% confidence level. More general than looking for shifts between populations is to ask whether each population samples the same underlying distribution. We use the non-parametric Kolmogorov–Smirnov test to find the likelihood that two datasets are drawn from the same distribution (the null-hypothesis). The results of the Kolmogorov–Smirnov test are presented in Table 3. Again, it is only the Pb isotopes which consistently distinguish between neovolcanic zones at a greater than 95% confidence level.

A second systematic pattern in Fig. 5 is in the shape of the distributions. Data points should align along the black lines in Fig. 5 if sampling a normal distribution. For Sr and Nd isotopes all zones fall close to, or within several sigma, of the theoretical distribution. However, the Pb isotopic

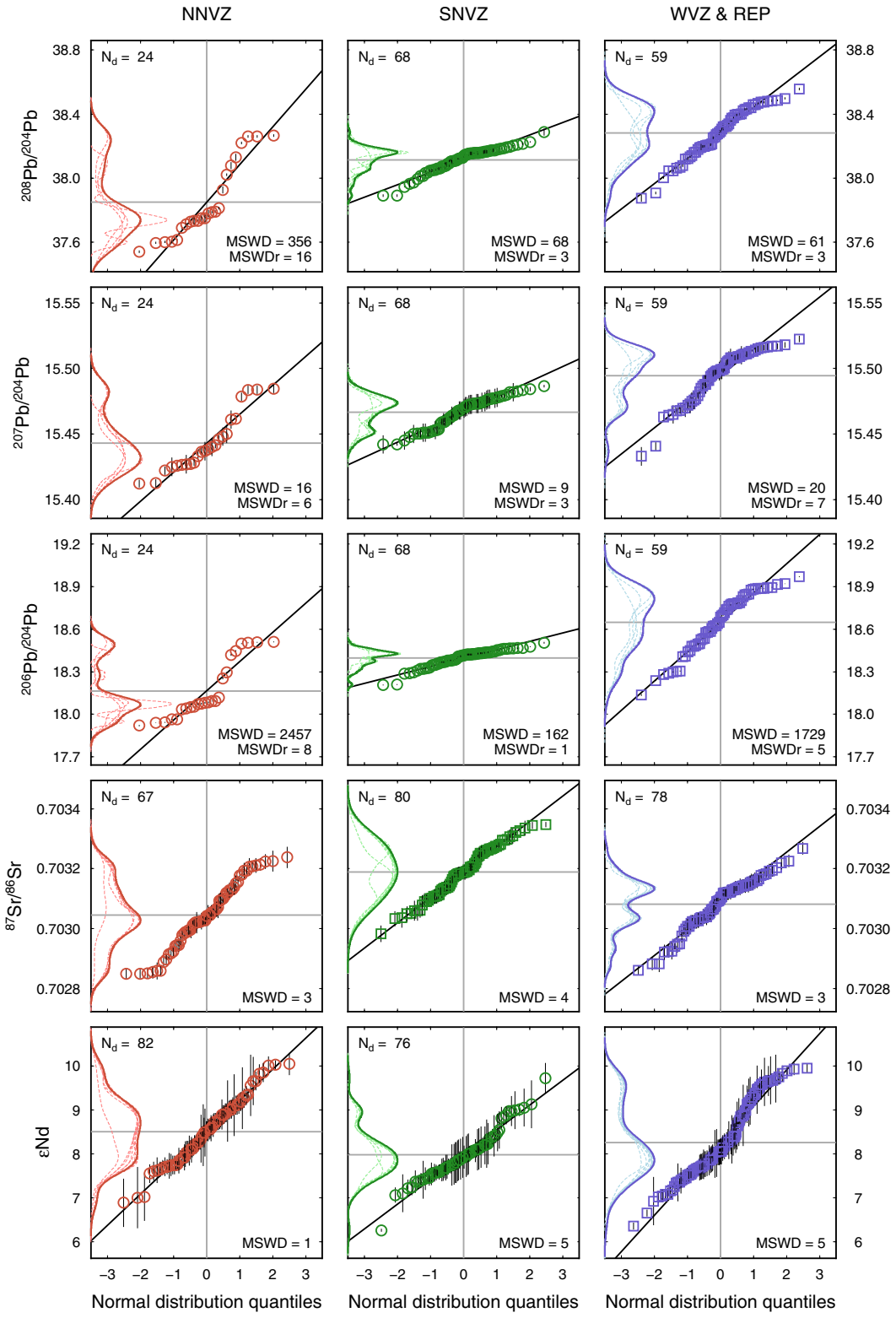

Fig. 5. Quantile–quantile plots comparing the shape of geochemical distributions from each zone against that predicted from a Gaussian distribution with the same mean and variance. If distributions are Gaussian, data should fall along the black line. Horizontal and vertical grey lines mark the distribution means. The mean square weighted deviation (MSWD) is a measure of how close each dataset is to the theoretical distribution and should equal one for a match within error of the data (2σ error bars drawn for each point). For Pb isotopes, MSWD is presented both in its regular format, where the weights used were the analytical uncertainty, and as MSWDr, where the weights have been scaled by the relative signal to noise of Pb isotopes compared with Sr and Nd isotopes. Also plotted are kernel density estimates of each distribution, which show the mode and skew of the distribution in a more familiar format. Dashed lines in each kernel density estimate are calculated by jackknifing as described in Section 2.3.3.

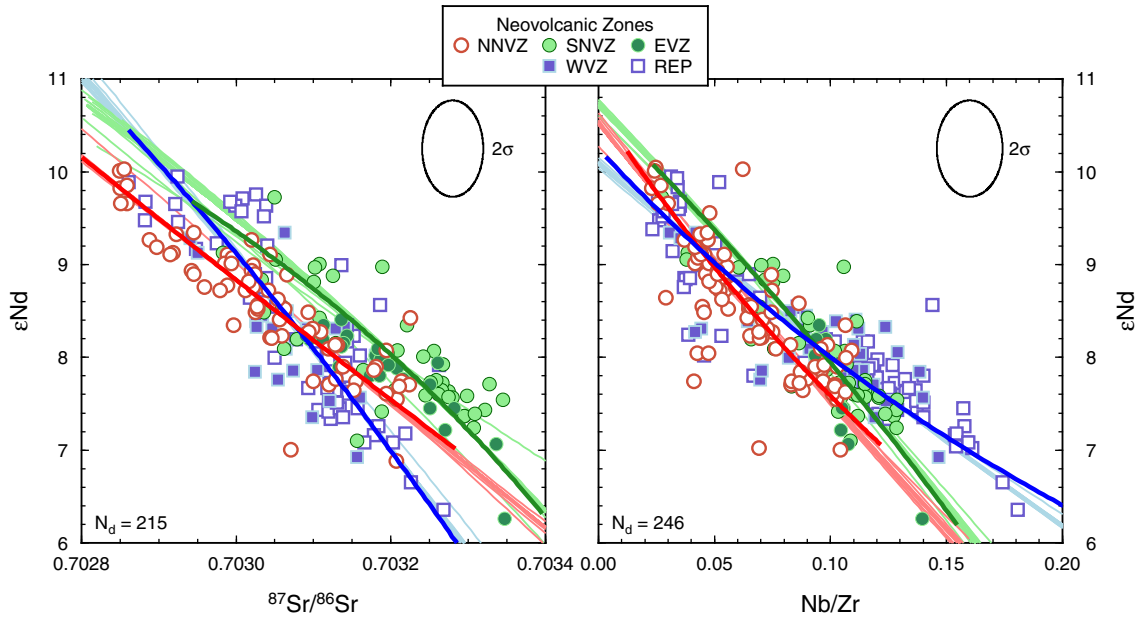

Fig. 6. Plots illustrating the Sr–Nd isotope and trace element mixing relationships on Iceland. Points are grouped by geographical location, with blue points from the west and south west of Iceland, green points from the east and centre and red points from the northeast. Also shown are binary mixing hyperbolae for the data grouped into its separate neovolcanic zones: thick lines mark the calculated regressions for the whole datasets, whilst thin lines are the jackknifed regressions—jackknifed according to the routine in Section 2.3.3. Binary mixing hyperbolae were calculated using the inversion scheme of Sohn (2005). Error ellipses are the mean for the input data.

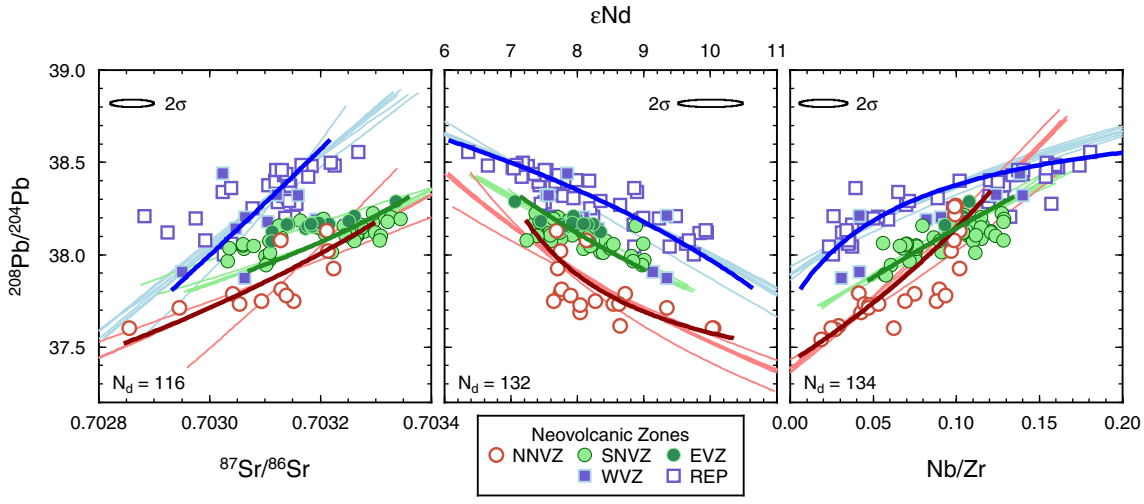

Fig. 7. Diagrams showing the ability of the Pb isotopes to split the samples from Iceland's different neovolcanic zones into distinct mixing arrays. Points are grouped by geographical location, with blue points from the west and south west of Iceland, green points from the east and centre and red points from the northeast. Also shown are binary mixing hyperbolae for the data grouped into its separate neovolcanic zones: thick lines mark the calculated regressions for the whole datasets, whilst thin lines are the jackknifed regressions—jackknifed according to the routine in Section 2.3.3. Binary mixing hyperbolae were calculated using the inversion scheme of Sohn (2005). Error ellipses are the mean for the input data.

compositions of samples from the NNVZ show a consistent skew, with the peak of distribution displaced to unradiogenic values. The WVZ/REP is closer to being normally distributed, but is slightly skewed towards radiogenic compositions. The skew of the chemical distributions is in effect what Thirlwall et al. (2004) were describing in identifying the infrequent presence of basalts with $^{206}Pb/^{204}Pb < 18.6$ (i.e. unradiogenic Pb) on the Reykjanes Peninsula. Fig. 5 shows that a similar but opposite pattern exists in the NNVZ data, where it is enriched samples that create a tail

Table 3
Percentage probabilities of the null hypothesis (H_0) being true, which for the Kolmogorov–Smirnov test is that the datasets being compared are drawn from the same distribution, whereas for the Mann–Whitney test H_0 is that the distributions do not differ by a systematic shift.[a]

Zone	Kolmogorov–Smirnov		Mann–Whitney		N_d
	NNVZ	SNVZ&EVZ	NNVZ	SNVZ&EVZ	
$^{206}Pb/^{204}Pb$					
NNVZ	–	–	–	–	24
SNVZ&EVZ	< 0.01	–	< 0.01	–	68
REP&WVZ	< 0.01	< 0.01	0.06 (1)	< 0.01	59
$^{207}Pb/^{204}Pb$					
NNVZ	–	–	–	–	24
SNVZ&EVZ	< 0.01	–	0.01 (4)	–	68
REP&WVZ	< 0.01	< 0.01	< 0.01	< 0.01	59
$^{208}Pb/^{204}Pb$					
NNVZ	–	–	–	–	24
SNVZ&EVZ	< 0.01	–	0.02 (4)	–	68
REP&WVZ	< 0.01	< 0.01	< 0.01	< 0.01	59
$^{87}Sr/^{86}Sr$					
NNVZ	–	–	–	–	67
SNVZ&EVZ	< 0.01	–	< 0.01	–	80
REP&WVZ	4 (5)	< 0.01	4 (9)	< 0.01	78
ϵNd					
NNVZ	–	–	–	–	82
SNVZ&EVZ	0.1 (8)	–	0.04 (7)	–	76
REP&WVZ	3 (11)	4 (3)	3 (8)	6 (4)	116

[a] Percentage probabilities have been calculated using the Kolmogorov–Smirnov test for two distributions (Press et al., 1992) and the statistical programming language R's built in function for two-sided Mann–Whitney tests. Both tests have been jackknifed as described in Section 2.3.3 to obtain a mean probability and its 1σ standard deviation, reported in parentheses as variation on the last digit.

in the distribution. In contrast to both the NNVZ and WVZ/REP, data from central Iceland are close to being normally distributed.

Most natural variation in Sr and Nd isotopic composition of basalts is at a much smaller level than is present in Pb isotopes. Given the analytical limitations of measuring isotope ratios very precisely, shifts in Sr or Nd isotopic compositions are less likely to be resolved than in Pb isotopes. The differences in the shape of the distributions observed in Fig. 5 between Pb and Sr/Nd isotopes could therefore be due to the lower signal to noise of Sr and Nd isotopes. A lower signal to noise would make it more likely that distributions appear Gaussian (from the central limit theorem). To test this we have calculated the mean square weighted deviation (MSWD) of data from the theoretical distributions twice: once using the real analytical precision of the data and a second time for Pb isotopes using their analytical uncertainty scaled by the relative signal to noise of Pb compared with Nd isotopes (MSWDr). The results of this calculation show that even accounting for the low signal to noise of Sr and Nd isotopes, Pb isotopes in the NNVZ and WVZ/REP have significant skew to their distributions.

In summary, this section finds robust spatial structure in the raw Pb isotope ratios of basalts. The Pb isotopic composition of basalts becomes progressively less radiogenic south to north across Iceland, with the NNVZ erupting on average the most unradiogenic basalts and the WVZ and REP the most radiogenic. Central Iceland lies between these two extremes. By contrast, Sr and Nd isotope ratios show no north–south spatial structure. Pb isotope distributions from the NNVZ and WVZ are significantly non-Gaussian, and are positively skewed towards radiogenic and unradiogenic compositions respectively. No departure from Gaussianity is observed in either Sr or Nd isotopes.

5. EVIDENCE FOR MULTIPLE GEOCHEMICAL ARRAYS ON ICELAND

Isotope data from suites of basalts are commonly used to define arrays, which can be read as having time significance (isochrons), or as being produced from variable proportions of mixing between two or more endmember compositions. We interpret the isotope–isotope arrays we present in this study as resulting from mixing between different endmember melt compositions. With this definition, defining data by the parameters of the array they fall upon (e.g. gradient and intercept) has a number of advantages over the univariate analysis presented above. Most importantly, whilst the univariate analysis can identify differences in mean composition, it is unclear whether these differences are due to varying mixing proportions between one set of radiogenic and unradiogenic endmembers, or whether the endmembers involved in mixing are themselves different between groups of data. Investigating which of these two processes gives neovolcanic zones their distinct composition is crucial in determining whether the same heterogeneities are distributed everywhere in the mantle, but present/sampled in different proportions, or whether some mantle compositions are only found in particular areas. In this section we estimate parameters defining the mixing arrays for Iceland's neovolcanic zones, and test

the mixing lines to see if common mixing endmembers can describe the isotopic variability.

5.1. Mixing arrays in ϵNd–^{87}Sr/^{86}Sr-trace element space

In the previous section Pb isotopes were shown to be exhibiting a spatial structure not resolvable in Nd and Sr isotopes. To determine whether bivariate analysis will expose spatially systematic behaviour in Nd and Sr isotopes we first assess the arrays formed by these isotopes independently from the Pb isotopes.

Fig. 6 plots the data from each neovolcanic zone in both ϵNd vs. ^{87}Sr/^{86}Sr space and ϵNd vs. Nb/Zr space. The negative correlations between ϵNd and Nb/Zr show that incompatible element enrichment in basalts is consistently correlated with the signal of radiogenic Sr and unradiogenic Nd. The coupling of incompatible trace element and isotope systematics will occur through a combination of process and source: (1) deep low degree melts have high Nb/Zr compared to their source due to the relative incompatibility of Nb with respect to Zr (Green et al., 1989; Ewart et al., 1998), (2) melts from enriched mantle domains inherit a high Nb/Zr from an intrinsically high Nb/Zr source and are the first melts to form beneath Iceland (Shorttle and Maclennan, 2011), (3) mixing between deep low degree peridotite melts (high Nb/Zr) and melts from a fertile source (high Nb/Zr, ^{87}Sr/^{86}Sr and low ϵNd) can generate the enriched endmember that goes onto mix with high degree melts of the more abundant depleted peridotite (Rudge et al., 2013). What is significant about the trace element-isotopic correlations in Fig. 6 for this contribution, is whether they pick out spatial differences in basalt chemistry.

The data from each neovolcanic zone in Fig. 6 form broad overlapping arrays, with departures from simple binary mixing largely controlled by analytical precision (see χ^2_r values in Table B.9 of the supporting material). Despite the low signal to noise of Sr and Nd isotopes, fitting binary mixing lines to the data shows that there are subtle differences in the zonal arrays (thick lines Fig. 6). The curvature of each neovolcanic zone's mixing array is statistically different (thin lines Fig. 6 and Table B.9), implying small differences in the trace element concentration of endmember melts between neovolcanic zones.

The difference between the binary mixing arrays from two neovolcanic zones can be formally assessed using an F-test. The reduction in misfit (measured as χ^2) achieved by fitting a separate regression to each neovolcanic zone's data is compared to the χ^2 of a single regression fitted to the combined dataset. The results of these comparisons for the mixing arrays in Fig. 6 are presented in Table 4. Despite the large amount of overlap between the arrays, there is enough data that each neovolcanic zone defines a statistically significant binary mixing hyperbola. Because mixing in Fig. 6 is non-linear, it is not simple to infer the geological implications of these statistically different mixing arrays. Either endmember elemental concentrations, endmember compositions, or both could be slightly varying to produce the distinct but overlapping arrays. Despite these zonal differences, little systematic pattern of spatial chemical structure emerges from Fig. 6.

Table 4
Percentage probabilities of H_0 being true, where H_0 is that data from the two neovolcanic zones are best fitted with a single binary mixing regression, rather than a separate regression for each zone.[a]

	NNVZ	SNVZ&EVZ	N_d
ϵNd vs. ^{87}Sr/^{86}Sr			
NNVZ	–	–	66
SNVZ&EVZ	< 0.01	–	72
REP&WVZ	0.01 (4)	< 0.01	77
ϵNd vs. Nb/Zr			
NNVZ	–	–	81
SNVZ&EVZ	0.03 (16)	–	59
REP&WVZ	0.3 (3)	0.02 (6)	106
^{208}Pb/^{204}Pb vs. ^{87}Sr/^{86}Sr			
NNVZ	–	–	12
SNVZ&EVZ	12 (7)	–	60
REP&WVZ	0.03 (7)	< 0.01	44
^{208}Pb/^{204}Pb vs. ϵNd			
NNVZ	–	–	18
SNVZ&EVZ	< 0.01	–	59
REP&WVZ	< 0.01	< 0.01	55
^{208}Pb/^{204}Pb vs. Nb/Zr			
NNVZ	–	–	24
SNVZ&EVZ	2 (6)	–	53
REP&WVZ	< 0.01	< 0.01	57

[a] Percentage probabilities have been calculated using an F-test with $N_d - 5$ and $N_d - 10$ degrees of freedom. Regressions coefficients were determined using Sohn (2005), with the procedure Jackknifed as described in Section 2.3.3 to obtain a mean probability and its 1σ standard deviation, reported in parentheses.

5.2. Mixing arrays involving Pb isotopes

The arrays defined by the Pb isotopes of Icelandic basalts are shown in Fig. 7. The parameters describing each of the binary mixing arrays in Fig. 7 can be found in Table B.9 of the supporting material. The data from each neovolcanic zone is described by binary mixing at the 99% confidence level (Table B.9). In Fig. 7 the offsets between each neovolcanic zone's geochemistry are identifiable not simply as differences in how radiogenic their basalts are, but also as defining distinct arrays: at a given value of ^{87}Sr/^{86}Sr or ϵNd, the corresponding Pb isotopic composition of basalts becomes less radiogenic south to north across Iceland (Fig. 7). In addition to offsets between the arrays, array curvature also varies systematically across Iceland. In each mixing array of Fig. 7, the NNVZ array has a significantly different and opposite curvature to the REP/WVZ array (Table B.9). The implication of the array curvatures is that the concentration ratio $[\mathrm{Pb}/(\mathrm{Sr},\mathrm{Nd},\mathrm{Zr})]^{\mathrm{enriched}} < [\mathrm{Pb}/(\mathrm{Sr},\mathrm{Nd},\mathrm{Zr})]^{\mathrm{depleted}}$ for NNVZ endmembers, whilst for REP/WVZ endmember melts $[\mathrm{Pb}/(\mathrm{Sr},\mathrm{Nd},\mathrm{Zr})]^{\mathrm{enriched}} > [\mathrm{Pb}/(\mathrm{Sr},\mathrm{Nd},\mathrm{Zr})]^{\mathrm{depleted}}$. Data from central Iceland consistently define an array with curvature intermediate between that of REP/WVZ and the NNVZ, and within 2σ of 1. However, the limited range in isotopic composition of central Iceland basalts means that the curvature of its arrays is poorly defined.

Table 4 records the significance of fitting separate binary mixing arrays to each neovolcanic zone's data. Because of the small amount of data in the NNVZ mixing array, in

both Pb–Nd and Pb–Nb/Zr space the difference between central Iceland and the NNVZ is not always significant at the 95% level. However, offset between the NNVZ and SNVZ/EVZ is clearly present in Pb–Nd space, and the NNVZ and REP/WVZ are consistently found to be different to one another.

Analysing the data in Pb–Pb isotope space has a number of advantages over the above univariate and bivariate approaches. Most importantly, if data is grouped such that mixing between two endmembers is the dominant process affecting basalt compositions, then the parameters calculated to define the array should not be very sensitive to sampling bias. Another factor is the identification of endmember compositions. Binary mixing in which the denominator of the ratios considered is not the same will produce curved mixing trends. Even with a constant endmember isotopic composition, curved mixing arrays are sensitive to changes in the melting process as different elemental concentrations of the endmembers will change the curvature of the data array. If data arrays shift around in Sr–Pb, or Nd–Pb space there is thus the possibility of misidentifying what could be changes in melting process as changes in source characteristics. Conversely, Pb isotopes will always exhibit linear mixing relationships in a two endmember system, and so shifts in the array can only be due to changes in the isotopic composition of the endmember melts (and therefore the source). Taken together these factors make the Pb isotope system much more powerful for resolving changes in mantle source than either Sr or Nd isotopes.

The Pb isotope data for all of Iceland's neovolcanic zones and two flank zones (Snæfellsnes and the southern EVZ) are presented in Fig. 8: Pb isotope ratios have been normalised to ^{206}Pb to remove the effect of spurious correlation potentially arising from normalisation to the low abundance 204 isotope. The curvature of the Icelandic Pb

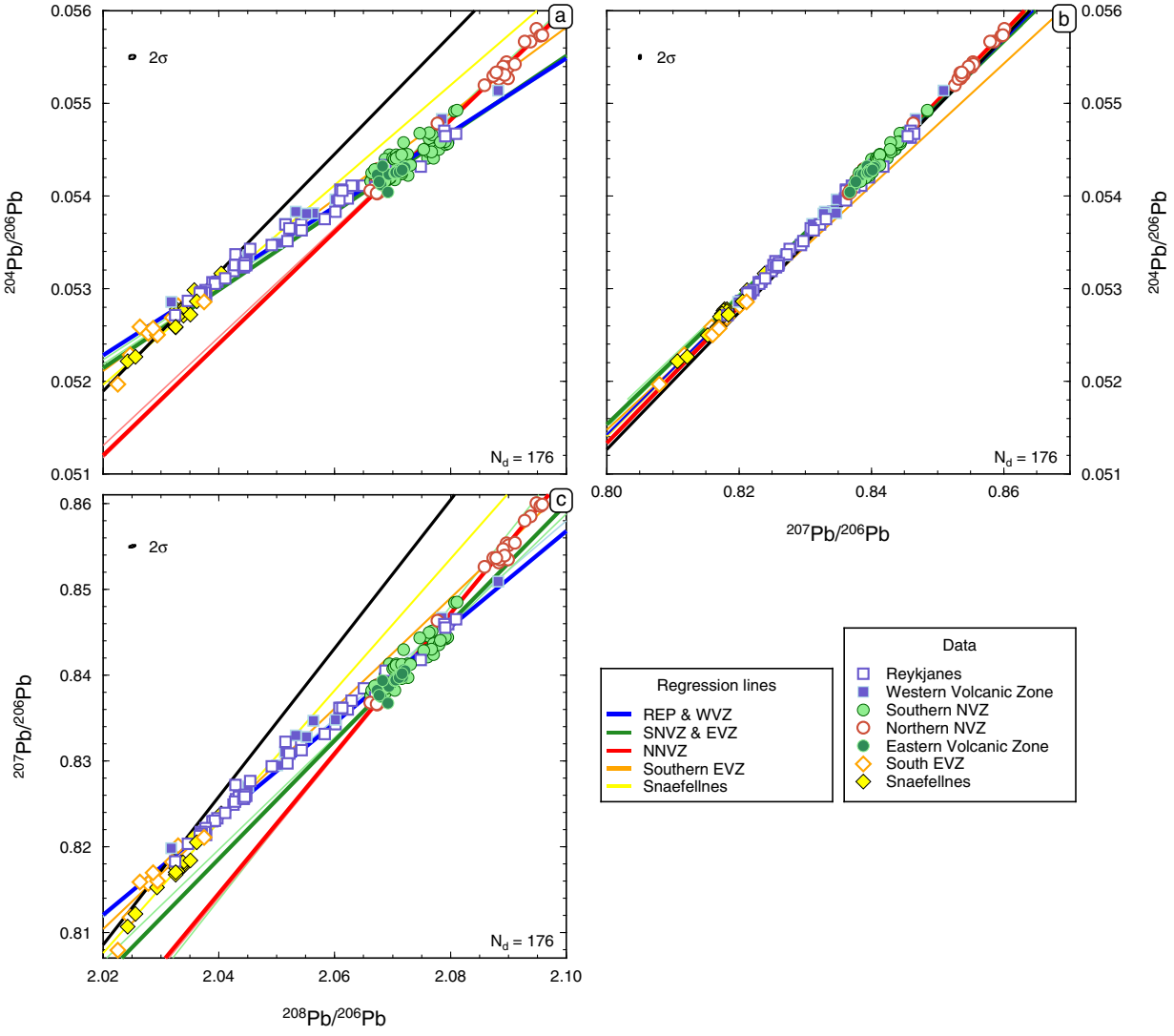

Fig. 8. (a–c) Raw Pb isotope data from Iceland's neovolcanic zones and two flank zones (Snæfellsnes and southern EVZ). The thick black line is Northern Hemisphere Reference Line (Hart, 1984); thick coloured lines are regressions for subsets of the data divided by neovolcanic zone, whilst thin lines are the jackknifed regression estimates—jackknifed according to the routine described in Section 2.3.3.

isotope array, noticed by previous authors (Peate et al., 2010), is clearly present when the thoranogenic ^{208}Pb isotope is included in one of the ratios (Fig. 8a and c). Colouring the data by neovolcanic zone indicates that the main bend in the isotope array occurs where the NNVZ and REP/WVZ data intersects, and is also where the central Iceland data clusters. The distinct arrays comprising the Icelandic Pb isotope data are drawn on for each neovolcanic zone as thick lines (Fig. 8) and the regression parameters given in Table B.10 of the supporting material. All regressions are found to be significant against the null-hypothesis of no correlation at a 99% confidence level, and the calculated R^2 values indicate that binary mixing accounts for a majority of variability in the data (Table B.10).

Binary mixing lines drawn on Fig. 8 show a clear difference between the mixing relationships of NNVZ basalts, and those of REP/WVZ basalts. More subtle is the difference between the central Iceland and NNVZ data, but use of the F-test indicates significant differences exist between all three neovolcanic zones' Pb isotope systematics (Table 5). A second bend in the Icelandic Pb isotope array, making it sigmoidal, is clear when the flank zone data are included. The flank zone data lies at the most radiogenic compositions (low ^{208}Pb/^{206}Pb, ^{207}Pb/^{206}Pb and ^{204}Pb/^{206}Pb), and defines arrays distinct from any of the neovolcanic zones (Table 5).

The results of the F-tests in Table 5 imply that each neovolcanic zone (REP/WVZ, SNVZ/EVZ and NNVZ) has not only a distinctive mean Pb isotopic composition, but also a characteristic mixing array in Pb isotope space. The identification of different mixing arrays is evidence for different endmember melt compositions supplying each of Iceland's neovolcanic zones. The lack of convergence between the on-land Iceland arrays at any depleted or enriched extreme also means that neither the enriched nor depleted endmember of the neovolcanic zones can be entirely common between them. Clearly a minimum of three endmember compositions are required to explain the variability in Fig. 8a and c, but it is possible that an arbitrarily greater number are in fact involved, and that mixing during melt extraction is creating the appearance of binary mixing (for example, the homogenisation of early stage enriched melts (Rudge et al., 2013)), or 'pseudo-endmembers' (Douglass and Schilling, 2000).

Despite binary mixing explaining a large proportion of variance in the Pb isotope data, the high values of χ^2_r in Table B.10 (all > 100) show that the data's average deviation away from the linear model is many times outside its analytical uncertainty. The arrays we define in Pb isotope space are therefore effectively the mixing equivalent of error-chrons, where there is significant geological noise unexplained by the simple linear model (Brooks et al., 1972). Part of the inadequacy of simple linear models in fitting the data may be from our initial assumptions of how to group the data, creating a spatial grouping of samples that is too coarse. In the following section we address this problem by calculating local statistical parameters.

6. SPATIAL STATISTICS

From the statistical analysis of Iceland's geochemical data we have found that the Pb isotopic composition of basalts shows a unique sensitivity to spatial location: this is apparent from the mean Pb isotopic composition and the binary mixing array Pb isotopes define either in Pb–Pb or Pb–Sr, Nd, Nb/Zr space. By grouping data by neovolcanic zone it appears these compositional shifts occur systematically north to south across Iceland. However, there were hints from the high χ^2_r of the Pb isotope binary mixing arrays that the zonal groupings we have defined

Table 5
Percentage probability of H_0, where H_0 is that the data from two neovolcanic zones in Pb–Pb space are best fitted with a single linear regression, rather than a separate linear regression for each zone.[a]

Zone	NNVZ	SNVZ&EVZ	REP&WVZ	sEVZ	SNFS
$^{208}Pb/^{206}Pb$ *vs.* $^{207}Pb/^{206}Pb$					
SNVZ&EVZ	0.3 (5)	–	–	–	–
REP&WVZ	< 0.01	< 0.01	–	–	–
sEVZ	< 0.01	0.02	6.61	–	–
SNFS	< 0.01	0.08	< 0.01	< 0.01	–
$^{208}Pb/^{206}Pb$ *vs.* $^{204}Pb/^{206}Pb$					
SNVZ&EVZ	1 (5)	–	–	–	–
REP&WVZ	< 0.01	9 (6)	–	–	–
sEVZ	< 0.01	73.20	0.29	–	–
SNFS	< 0.01	22.44	< 0.01	1.69	–
$^{207}Pb/^{206}Pb$ *vs.* $^{204}Pb/^{206}Pb$					
SNVZ&EVZ	4 (16)	–	–	–	–
REP&WVZ	0.1 (3)	0.4 (7)	–	–	–
sEVZ	1.22	0.76	7.96	–	–
SNFS	7.77	7.18	70.49	0.64	–
N_d	24	68	59	9	16

[a] Percentage probabilities have been calculated using an F-test with $N_d - 2$ and $N_d - 4$ degrees of freedom. Linear regression parameters are calculated using York (1969). The regressions were Jackknifed as described in Section 2.3.3, to obtain a mean probability and 1σ standard deviation, reported in parentheses. Jackknifing has not been carried out for comparisons including the sEVZ and SNFS zones because the available datasets are too small.

are too coarse, causing us to miss significant local variability in regression gradient or mean composition. To gain this local information, and in order to place direct constraints on the scale and structure of spatial geochemical variability, it is necessary to interrogate the data directly in the spatial domain.

A sense of the spatial structure in Iceland's isotopic data can be seen from the maps in Fig. 9. In each map samples have been plotted according to their location and coloured by their isotopic composition. Most striking is the difference in location of extreme values for each isotope system. For Sr and Nd isotopes, the most radiogenic compositions occur in basalts erupted in the Snæfellsnes flank zone, and to a lesser degree in the southern EVZ. Within the neovolcanic zones Sr and Nd isotopes look as though they scatter about the same mean composition wherever they are sampled. In contrast, Pb isotopes show clear spatial structure: the flank zones basalts are still radiogenic extremes, but now the REP/WVZ basalts extend to almost as radiogenic values as the south EVZ and Snæfellsnes basalts and compositions clearly grow more depleted towards the north of the island (Fig. 9). So whilst changes in tectonic setting (i.e. flank vs. rift zone) strongly affect the Sr and Nd isotopic signal of basalts, the Pb isotopic composition appears to be at least equally sensitive to spatial location as it does tectonics. In trying to resolve the chemical structure of the Icelandic mantle, we want to control for tectonics as much as possible. For this reason we focus our subsequent analysis on samples from the main rift zones.

The maps in Fig. 9 indicate the limits of spatial resolution that spatial statistical methods will achieve. East of the REP from 20°–21°W and ~ 64°N there are a group of samples coloured orange in the $^{208}Pb/^{206}Pb$ map of Fig. 9. These samples are from the Thjorsarhraun flow, which travelled ~ 140 km from central Iceland to arrive at the island's southern coast (Halldorsson et al., 2008). The geochemical consequence of lateral transport is that Thjorsarhraun basalts with a mean $^{208}Pb/^{206}Pb \approx 2.07$ are juxtaposed with those from the Reykjanes Peninsula with a mean $^{208}Pb/^{206}Pb \approx 2.04$. So spatial shifts in basalt composition that would otherwise require > 100 km of movement along-ridge to see, occur in ~ 20 km. Whilst the Thjorsarhraun flow is an extreme example, all lava flows laterally redistribute the chemical signal they acquire from the mantle. One way to mitigate the effect would be to correct all sample locations back to the eruptive vent from which they derive. However, when the eruptive vent is a fissure, as in the case of some of Iceland's recent large volume flows (e.g. Skaftáreldar/Laki), there is no single point of eruption to return samples to. A more basic problem is that for some flows the location of the vent is not known (e.g. Thjorsarhraun (Halldorsson et al., 2008)). Although correcting back to a single point of eruption is clearly not simple, even with the above limitations a correction could be made to an accuracy of < 10 km. However, lateral transport of geochemical signals at the surface of the Earth is only a small part of the problem. Magma transport is also occurring in the crust and mantle to both focus magma from a wide melting zone to a narrow neovolcanic rift, and redistribute magma parallel to the ridge axis (Björnsson et al., 1977; Kelemen et al., 1997). In general there is no way of knowing how much deep lateral movement of magma has taken place, which means relocating lavas to their eruptive vent cannot fully resolve the problem.

Despite the above caveats, the maps in Fig. 9 and previous univariate and bivariate analyses show that basalt compositions are spatially systematic and so most lateral redistribution that does occur must itself be spatially restricted. By interrogating Iceland's geochemical data in the spatial domain we hope to constrain the length scale of spatial structure and how spatial structure depends upon the geochemical tracer used to map it.

6.1. Spatial autocorrelation

A measure of the global spatial structure in a dataset is provided by Moran's *I*, which calculates the spatial autocorrelation of observables (Moran, 1950). Spatial

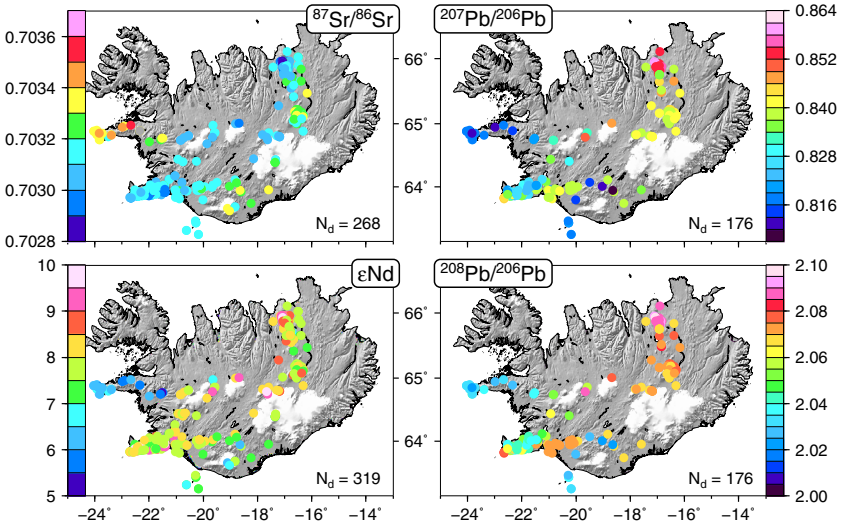

Fig. 9. Maps of the isotopic composition of basalts as a function of sampling location on Iceland. Points are coloured according to isotopic composition and plotted where the sample was collected. Data sources in Table B.7.

autocorrelation provides a measure of the similarity or dissimilarity of spatially proximal points. Perfect spatial dispersal of a signal (e.g. a chess board pattern) will be indicated by $I = -1$, a positive spatial autocorrelation (clustering of similar valued data points) will in general give $I > 0$, and for a random distribution of signal $I = 0$. Moran's I is calculated as,

$$I = z^T Wz/(z^T z) \quad (1)$$

where z is the standardised data vector (mean subtracted and divided by standard deviation), and W is the row normalised spatial weights matrix with $w_{ii} = 0$. More information and definitions can be found in E. In Table 6 the Moran's I values calculated for Iceland's Pb, Sr and Nd isotopes are given, with error estimates calculated from jackknifing and significance levels on the estimates of autocorrelation. To avoid the potential of multiple samples from the same eruption creating the false appearance of spatial autocorrelation, all calculations of Moran's I have been carried out on a dataset containing only a single average composition for each eruption.

The first three rows of Table 6 have Moran's I values calculated on data from all of Iceland's neovolcanic zones and for two regional subdivisions. Pb isotopes show the strongest spatial autocorrelation and are the only isotope system to have significant autocorrelation for each grouping of data. However, all three isotope systems do show some degree of positive spatial autocorrelation, meaning that the Sr, Nd, and Pb isotopic composition of nearby eruptions tend to be more similar to each other than they do to more distal eruptions. This result is important because it demonstrates the significance of location in determining the isotopic character of a basalt. The dependence of composition on location persists when the data are subdivided by region and I recalculated (second and third rows Table 6), although it is weaker than when all of Iceland is considered at once. The weakening of spatial autocorrelation when I is calculated from single regions indicates that a large part of the positive autocorrelation is coming from island-scale geochemical structure—such as the progressively less radiogenic Pb isotope compositions south to north across Iceland (Fig. 9). That Sr and Nd isotopes have significantly weaker spatial autocorrelation than Pb isotopes on an island-scale, but more similar I-values to the Pb isotopes on a local scale, implies that the strongest decoupling between Pb and Sr/Nd occurs on length scales > 100 km. The Nd and Sr isotopes also show smaller relative decreases in I as the spatial scale of data inclusion is decreased. Nd isotopes in particular exhibit a very minor reduction in I, demonstrating that the structure of Nd isotopes is similar on length scales both > 100 km and < 100 km. The presence of positive spatial autocorrelation on a local scale also hints that the groupings used in the univariate and bivariate analysis in Section 4 above may have been too coarse.

As mentioned previously, Pb isotopes have a significantly higher signal to noise ratio (SN) than Sr/Nd isotopes. The effect of a low SN for Sr and Nd isotopes could be to mask spatial autocorrelation present in their real spatial distributions. To assess whether SN is controlling the differences in I between Pb and Sr/Nd isotopes, rows 4–9 of Table 6 recalculate I by Monte-Carlo simulation, permuting the Pb isotope composition on each point by its quoted analytical uncertainty scaled by $SN^{Pb}/SN^{Sr,Nd}$. Table 6 shows that even when the signal to noise of Pb isotopes is reduced, the spatial autocorrelation observed in the all Iceland grouping persists at a level greater than that seen in the raw Sr and Nd isotope data. The greater spatial autocorrelation of the Pb isotopes compared with that of Sr/Nd isotopes is therefore a real feature of the geochemistry of Icelandic basalts on an island-scale and not an artifact of analytical precision. On the scale of a neovolcanic zone, however, the reduction in signal to noise brings I^{Pb} down to similar values to I^{Sr} and I^{Nd}—implying that at this length scale the contrasting strength of spatial autocorrelation between the isotope systems is largely attributable to differences in signal to noise.

Table 6
Moran's I measure of global spatial autocorrelation of isotopic observables for Iceland's neovolcanic zones, calculated on the real data and for tests where the signal to noise of the Pb isotopes is reduced to that of Sr and Nd isotopes.[a]

	$^{208}Pb/^{206}Pb$	$^{207}Pb/^{206}Pb$	$^{204}Pb/^{206}Pb$	$^{87}Sr/^{86}Sr$	ϵNd	N_e
Raw data						
All	0.59 (4,0)	0.60 (5,0)	0.62 (5,0)	0.20 (5,0)	0.06 (1,2)	69
SNVZ&EVZ	0.21 (6,0)	0.20 (6,0)	0.13 (5,0)	0.11 (3,0)	0.06 (1,0)	22
REP&WVZ	0.09 (3,0)	0.10 (3,0)	0.10 (3,0)	0.03 (1,7)	0.05 (2,1)	37
Signal:noise reduced to that of $^{87}Sr/^{86}Sr$						
All	0.46 (2,0)	0.46 (3,0)	0.59 (5,0)	–	–	69
SNVZ&EVZ	0.09 (3,0)	0.08 (3,0)	0.10 (4,0)	–	–	22
REP&WVZ	0.08 (2,0)	0.09 (2,0)	0.10 (3,0)	–	–	37
Signal:noise reduced to that of ϵNd						
All	0.37 (2,0)	0.36 (2,0)	0.56 (4,0)	–	–	69
SNVZ&EVZ	0.10 (2,1)	0.11 (2,1)	0.12 (3,0)	–	–	22
REP&WVZ	0.09 (2,0)	0.09 (2,0)	0.10 (3,0)	–	–	37

[a] 'All' refers to the neovolcanic zones: NNVZ, SNVZ, EVZ, WVZ and REP. The number of unique eruptions used in each spatial grouping is N_e. Given in parentheses is the 1 sigma standard deviation on the last digit of I, followed by the percentage probability of the null hypothesis being true that there is no spatial autocorrelation—both the error on I and percentage probability are calculated following the jackknifing routine in Section 2.3.3. An adaptive weighting function was used for the calculating Moran's I such that at least ten points are within one bandwidth, further details can be found in E.

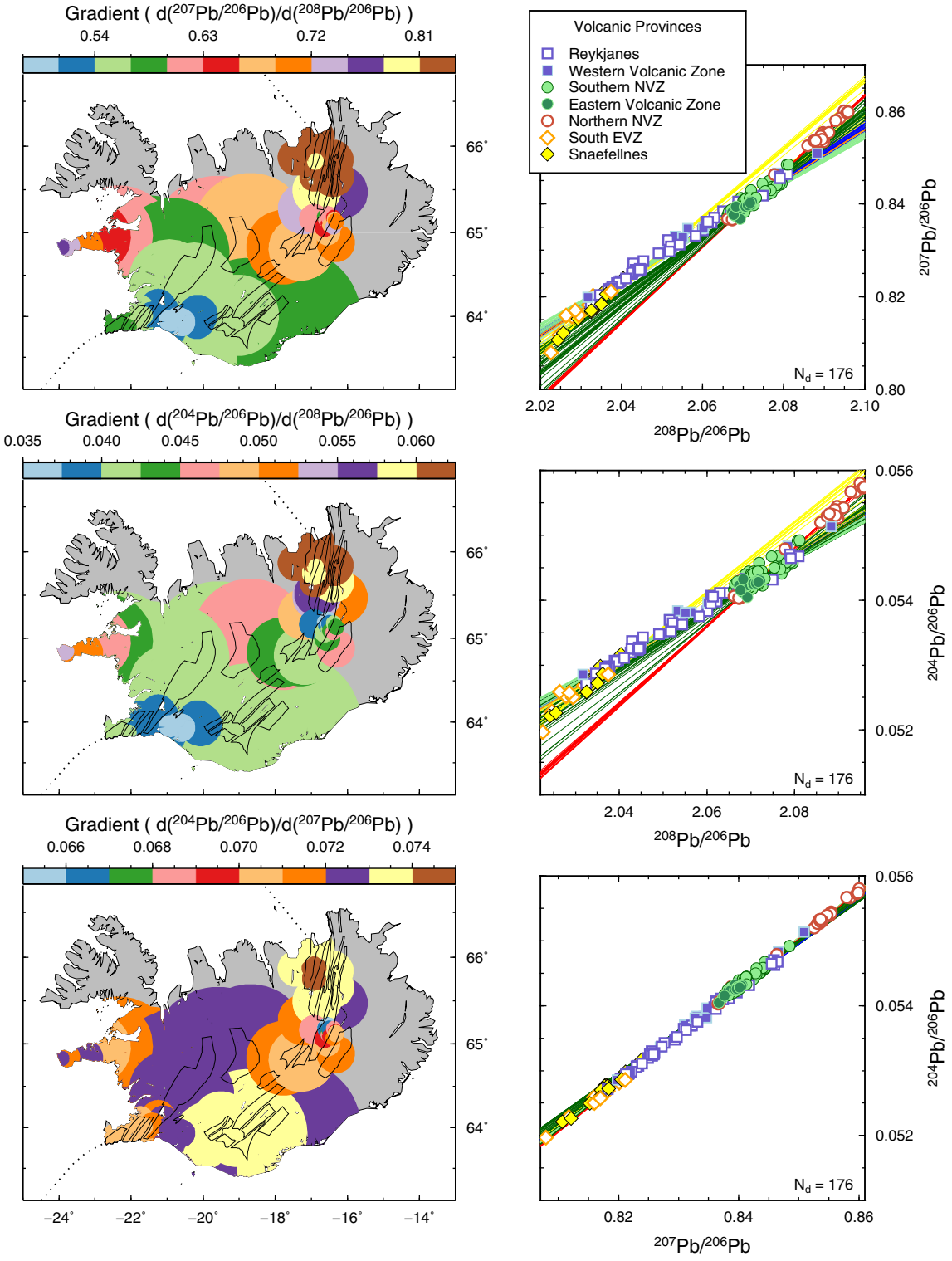

Fig. 10. Results of performing geographically weighted regression in Pb isotope space. Maps of the calculated regressions are shown in the left column and isotope–isotope plots of all the regression solutions in the right column. At each data point local regression parameters have been calculated, weighting all other data points in the regression according to geographic distance from the central sample point. The bandwidth of the Gaussian weight function varies according to sampling density, so that at least 10 data points are within one bandwidth; the size of the circles on the map have a radius equal to the local bandwidth used. The value of calculated local regression parameters at each point is indicated by the colour of the circle.

6.2. Geographically weighted regression

The Moran's I statistic calculated above is a univariate analysis in the spatial domain, returning a single 'global' value of spatial autocorrelation (Anselin, 1995). One limitation of the global Moran's I is that it does not retain specific information about local spatial structure. A second limitation is that Moran's I is calculated on univariate datasets, whilst Section 5 demonstrated that spatial structure exists not only in mean composition, but also in geochemical mixing array. One statistical method which can overcome the drawbacks of Moran's I is geographically weighted regression (GWR; Fotheringham et al., 2002). GWR uses a conventional weighted linear regression algorithm to calculate the model parameters for a dataset. In this case we use the routine of York (1969). The innovation of GWR is that in addition to weighting the geochemical data by their analytical uncertainty an extra weight term is applied that makes the regression sensitive only to samples from a local area.

Using GWR, we calculate local regression parameters around every sample location in our dataset. Weighting is applied so that the central data point has a weight of one and all other points gain an exponentially decaying weight as a function of their distance from the centre—full details of the GWR scheme we use are included in Appendix F. The result of applying GWR to a dataset is to obtain a pair of regression parameters (gradient and intercept) for every data point, each pair defining a local binary mixing array. Instead of mapping the raw geochemical data as in Fig. 9, the regression parameters derived from that data can be mapped and assessed for spatial structure. GWR is only applied to data in Pb–Pb space. Partly this is because the previous statistical analyses demonstrate that only Pb isotopes show consistent spatial structure. But also, restricting the analysis to Pb isotopes means that the arrays unambiguously define endmember melt compositions. Characterising a change in mixing endmember is a more fundamental result than is often achievable from Pb–Sr or Pb–Nd regressions.

Fig. 10 presents the maps of local regression parameters calculated in Pb–Pb isotope space. For each sample location a circle is plotted equal in dimension to the bandwidth used to apply the geographic weight, with small circles plotted on top of larger circles. The weights are varied so that at least 10 samples are within one bandwidth, meaning that where the sample density is low the bandwidth is large. The size of the circles in Fig. 10 show that the sample density in the WVZ, EVZ, and southern EVZ is low, whilst the REP, SNVZ, and NNVZ are relatively well sampled. The circles are coloured by the value of gradient determined in the local regression analysis, with scale bars given at the top of each map.

The distribution of colours in the $^{207}Pb/^{206}Pb$ vs. $^{208}Pb/^{206}Pb$ and $^{204}Pb/^{206}Pb$ vs. $^{208}Pb/^{206}Pb$ maps records the changing gradient in Pb isotope space north to south across the island (Fig. 10). In each of these maps, central and northern Iceland are marked by consistently different colours compared with south and south west Iceland, and the colours change progressively from NNVZ–SNVZ/EVZ–REP/WVZ. In $^{204}Pb/^{206}Pb$ vs. $^{207}Pb/^{206}Pb$ space (bottom row of Fig. 10), there is less obvious systematic spatial structure to the local regression gradient: consistent with the F-tests reported in Table 5, where the p-values for comparison between zonal regressions are generally higher in $^{204}Pb/^{206}Pb$ vs. $^{207}Pb/^{206}Pb$ space (i.e. the regressions are more similar) compared with the other two Pb–Pb isotope plots. This result is further evidence that the spatial structure in regression parameters is being defined by ^{208}Pb.

7. RECONCILING DIVERSE SPATIAL OBSERVATIONS

From the above statistical analyses we found two forms of spatial structure: (1) A change in mean Pb isotopic composition from radiogenic values in the south, to progressively unradiogenic values in the north of Iceland; and (2) a shift in binary mixing array occurring on a length scale of $\sim$ 160 km, identifiable in Pb–Pb and Pb–Sr, Nd space. One conclusion to draw from these observations is that Pb isotope systematics are decoupled from those of Sr and Nd isotopes. However, on a short enough length scale these systems are correlated: our new data, and that of Stracke et al. (2003), Thirlwall et al. (2004), Peate et al. (2009, 2010), show that in spatially-restricted datasets Pb isotopes follow the enrichment–depletion trend of incompatible trace elements and Sr and Nd isotopes (Fig. 3). An important question then, is on what length scale the Pb isotopes and the other geochemical observables decoupled? To identify a length scale of decoupling it will be necessary to express each type of observation (raw isotopic composition, GWR parameter, etc.) such that they can be directly compared, and tested for significance against a null hypothesis of no spatial structure. Having the differing types of spatial structure expressed in the same way will also allow their relative magnitude and significance to be determined, and for constraints to be placed on the underlying geochemical distribution generating the spatial patterns.

A common means of expressing spatial structure can be found if observables (e.g. regression parameter or isotopic composition), instead of being directly mapped, are interrogated in terms of how much they change over space. If geochemical parameters exhibit island-scale spatial structure then they may be more different at large separation distances (coast–coast) than at short separation distances (adjacent lava flows): conversely, a uniformly-heterogeneous observable will show the same similarity between samples at all scales of comparison. These two extremes of uniform-heterogeneous vs. island-scale structure suggest that the way to obtain a length scale of variability is to compare the geochemical parameters between all samples and group the comparisons by sample–sample distance: if there is a non-uniformly-heterogeneous geochemical distribution then the geochemical similarity of samples will depend upon the distance of comparison. Below we describe a method for relating the geochemical similarity of all sample pairs in a dataset to their separation distance and how the resulting distributions can be interpreted in terms of spatial structure.

7.1. Constructing a distribution to describe spatial structure

In a regional geochemical dataset there are multiple length scales of comparison that can be explored, as each sample can be paired with every other and the geochemical similarity of every pair quantified. For a dataset of N_d samples there are $N_d(N_d-1)/2$ unique sample–sample pairings, each with associated parameter misfits measuring the similarity of observables between the sample pairs. If these sample pairs are then ordered by increasing separation distance a cumulative distribution of misfit can be calculated, the shape of which will be sensitive to the length scale of sample–sample comparison at which parameters are most different. We use a chi-squared type metric to quantify the misfit between sample parameters so that raw differences are scaled by their uncertainty—in this way misfit between parameters that is attributable to analytical noise is given a low weight in the summation. The chi-squared from individual ith–jth sample pairs, is calculated as

$$\chi^2_{ij} = (C_i - C_j)^2/(\sigma_i^2 + \sigma_j^2), \tag{2}$$

for all unique sample pairings, where C_i is the value of an observable (e.g. isotopic composition), and σ_i is that observation's associated one standard deviation uncertainty (e.g. analytical precision). To calculate a cumulative distribution the χ^2_{ij} are ordered according to the distance d_{ij} between the samples, then the cumulative chi-squared up to each distance r calculated as

$$X^2_r = \frac{\sum_j \sum_{i>j, i\neq j} \chi^2_{ij}}{X^2_t} \text{ for all } d_{ij} \leqslant r, \tag{3}$$

where $X^2_t = \sum_j \sum_{i>j, i\neq j} \chi^2_{ij}$ over all d_{ij}. When the observable is a spatial average, such as a GWR parameter, the effective sample–sample distance $\hat{d}_{ij}$ is used instead of d_{ij} (see Appendix D). To compare between spatially averaged parameters and raw isotopic compositions we calculate spatial means of the isotopic data using the same bandwidths as used in the GWR.

7.2. Results of cumulative chi-squared analysis

In Fig. 11a we calculate the cumulative chi-squared distributions for the raw isotopic observables. The general form of these distributions is a rapid increase in X^2 up to $\sim$ 100 km, a shallower slope over 100–250 km, followed by a second rapid increase up to 1. Part of the shape of the X^2 curves depends upon the spatial distribution of samples, so in Fig. 11 we produce kernel density estimates of sample pairing density as a function of distance. These kernel density plots show that the peaks in sample–sample pairing distances occur at $\sim$ 20 km and $\sim$ 320 km, which are therefore responsible for the slope–flat–slope structure identified in the X^2 distributions. However, as the same selection of samples has been used for all isotopes in Fig. 11a, the offset between the Pb isotopes (black lines) and Sr and Nd isotopes (red and blue lines respectively) cannot be explained by sample distribution. By 100 km sample pairing distance Sr and Nd isotopes have accumulated $\sim$ 50% of the total chi-squared misfit they generate over the whole of Iceland. Conversely, by 100 km the Pb isotopes have only accumulated $\sim$ 25% of their total chi-squared misfit. The concave up Pb isotope X^2 profiles indicate that most of the difference in Pb isotopes is seen by sample–sample comparisons over long length scales—i.e. between the different neovolcanic zones—whilst for Sr and Nd isotopes local variability is similar to global variability.

The X^2 distributions can be tested for significant non-random spatial structure by repeatedly randomly redistributing all parameters between sample locations and recalculating new X^2s. This procedure creates a population of X^2 distributions for the null-hypothesis of there being no spatially systematic structure, from which a mean X^2 and standard deviation can be calculated at each sample pairing distance. Offsets between the real and null distributions can then be expressed as a z-score, with a z-score offset > 3 indicating significant difference at the 95% confidence level (see the caption to Fig. 11 for details). The z-score distributions for the raw isotopic observables are presented in Fig. 11d. The low z-score values for Sr and Nd isotopes demonstrates their cumulative chi-squared profiles are close to what would be predicted for an entirely random distribution of isotopic compositions. By contrast the Pb isotopes show statistically significant deviations from the null distribution, indicating their structure is spatially non-random. The maximum difference between the real and random Pb isotope distributions occurs at a sample pairing distance of $\sim$ 150 km.

To compare the spatial structure of GWR parameters with that of the raw isotopic observables requires the isotope data to be spatially averaged. Fig. 11b presents the X^2 distributions for each of the GWR derived Pb isotope gradients (yellow/orange lines) and the spatially averaged Sr, Nd and Pb isotopes. The concave up shape of the Pb isotope distribution, which previously distinguished it from the Sr and Nd isotope distributions, is now even more apparent. When averaged, the Sr isotopes have also begun to show similar structure to the Pb isotopes—with more than 70% of their total chi-squared misfit occurring at sample pairing distances of > 100 km. Local Pb isotope regression gradients produce increasingly concave up profiles in the order $d(^{207}Pb/^{206}Pb)/d(^{204}Pb/^{206}Pb)$, $d(^{208}Pb/^{206}Pb)/d(^{204}Pb/^{206}Pb)$ and $d(^{207}Pb/^{206}Pb)/d(^{208}Pb/^{206}Pb)$. Testing each of the X^2s against their respective null-hypothesis distributions produces the z-score profiles in Fig. 11e. Taking spatial averages has a general tendency to increase the significance of spatial structure in observables compared with random spatial distributions. However, the spatial parameters involving Pb isotopes all show more significant spatial structure than the other observables. Interestingly, the significance of the thoranogenic ^{208}Pb isotope in generating spatial structure is again suggested by the relative significance of the spatially averaged Pb isotope compositions ($^{208}Pb/^{206}Pb$ highest), and the local regressions ($d(^{207}Pb/^{206}Pb)/d(^{204}Pb/^{206}Pb)$ has the lowest significance). The spatial structure in the averaged Sr isotopic compositions is significant, and is possibly reflecting the slightly more radiogenic values found in central Iceland (e.g. Fig. 5). Peak significance for most observables occurs at

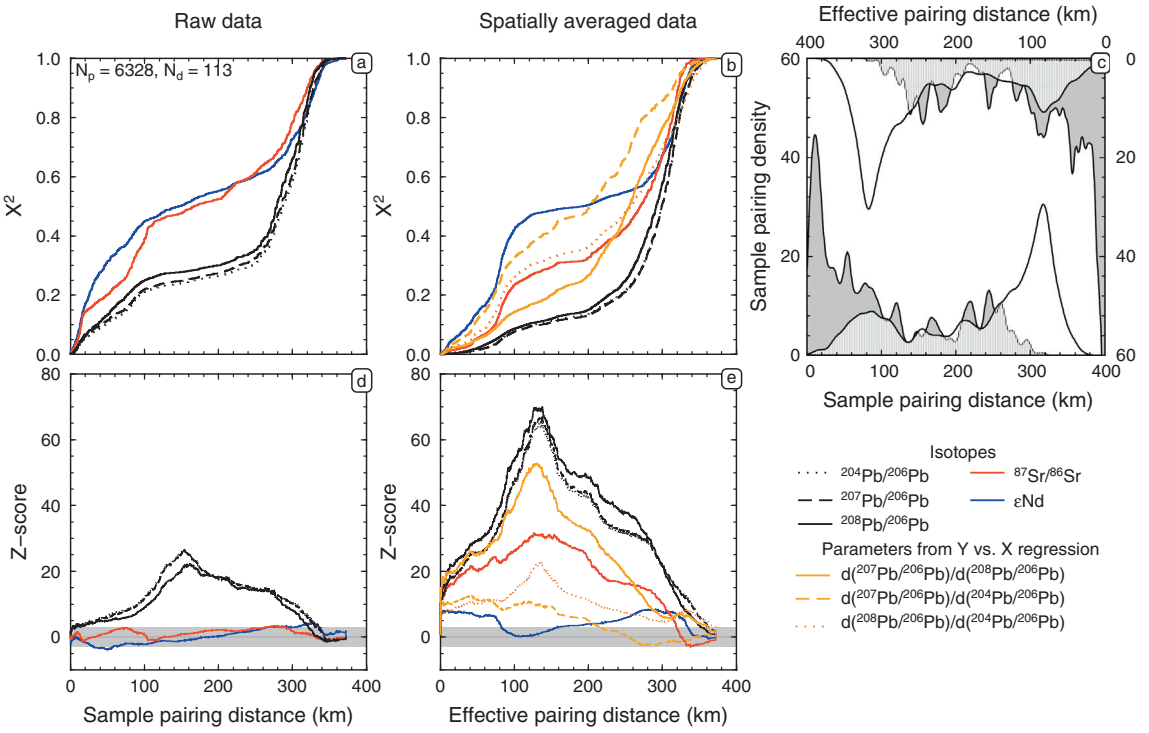

Fig. 11. (a) and (b) Cumulative chi-squared plots for Iceland's neovolcanic zones (NNVZ, SNVZ, EVZ, WVZ, REP), recording the rate at which the observed variance in a parameter increases as the sampling length scale is increased. Only samples younger than 80 ka and with joint Pb, Nd and Sr analyses were included. (d) and (e) Give the z-score significance estimates of the cumulative distributions, using a Monte-Carlo method in which the samples were randomly reassigned to spatial locations and the cumulative chi-squared re-calculated. Distributions outside the horizontal grey bar are significantly different from the null hypothesis of a random spatial distribution at the 95% level. Z-scores at a distance r were calculated as $z_r = (X_r^2 - \bar{X}_{0r}^2)/\sigma_r$, where $\bar{X}_{o_r}^2$ is the mean X^2 of the null distribution at a distance d and σ_r the standard deviation of the null distributions at that distance. For (b) and (e) all observables are spatial averages, and so effective sample distance is used in constructing X^2 (see D). (c) Kernel density plot of pairing distances. Bottom axis and distributions are real sample–sample distances, whilst top axis is effective pairing distances. Pairings are divided into REP/WVZ–NNVZ/SNVZ/EVZ in white, and pairings where both samples are from the same region. N_d records the total number of samples used, and N_p the number of unique permutations of those N_d samples. Further details can be found in the text.

$\sim$ 130 km effective pairing distance, similar to the length scale found from the raw isotopic data X^2 profiles.

7.3. Comparison of real and synthetic spatial distributions

The X^2 plots also enable comparison of the real distributions with synthetic spatial geochemical profiles. Matching synthetic profiles cannot generate a unique solution to Iceland's geochemical structure, but it can rule out certain possibilities and suggest plausible geometries. Synthetic profiles also help in understanding what spatial structure X^2 profiles are sensitive to. In Fig. 12 we examine four possible spatial structures: (1) a scenario where the average composition is uniformly-heterogeneous (left column Fig. 12); (2) the case where spatial structure is dominated by a Gaussian anomaly (central column Fig. 12); (3) a step change in isotopic composition between the REP/WVZ and SNVZ/EVZ/NNVZ, and (4) a systematic linear change in compositions over space (right column Fig. 12). From these four types of spatial structure two types of calculation have been performed: the first calculation samples the synthetic profiles with the real sample locations and adds noise to each pick in proportion to the analytical precision associated with each sample location. The second calculation type performs the same sampling of the synthetic profiles, but perturbs the picked value by a scaled analytical precision, scaled so that in a given location 40% of the total range in geochemistry across the island is within 1 sigma of the local mean. This latter scenario is meant to more closely resemble what we observe on Iceland, where although there are offsets in the mean value of geochemical parameters between neovolcanic zones there is also significant overlap between each zone's compositions. From these two types of sampling of the synthetic profiles we have repeatedly calculated cumulative chi-squared distributions and compared them with the real observations (see caption to Fig. 12 for details).

The Kolmogorov–Smirnov statistic, d(K–S), assesses cumulative distributions for similarity (Press et al., 1992), with smaller d(K–S) values indicating more similar distributions. We use d(K–S) as a measure of the success of the synthetic geochemical distributions in reproducing the X^2 of the real observations. Comparing d(K–S) between profiles shows that the raw Sr and Nd isotope X^2 distributions are best matched by a uniformly-heterogeneous underlying geochemical distribution: this is the case whether or not the cumulative chi-squared distributions are calculated

applying local noise. However, for the Pb isotope X^2 profile the uniformly-heterogeneous distribution provides a poor match to the real profile—uniform-heterogeneous distributions create too much variability at short length scales of sample comparison to match the slow increase of X^2 observed from the real Pb data. Sampling a Gaussian geochemical anomaly slightly improves the fit to the real Pb isotope X^2 and worsens it for Sr and Nd isotopes. A geochemical profile with either a step change in compositions between north and south Iceland, or an E–W linear increase (both with local noise), generates the most similar X^2 (third and forth columns of Fig. 11).

There will always be an arbitrarily large number of synthetic spatial distributions that can generate X^2 profiles similar to real ones. The non-uniqueness is demonstrated in our analysis, where both step function and planar increase distributions generate X^2 similar to the observed Pb isotopic profile—therefore, these two types of structure are not able to be distinguished by X^2 alone. The real utility of 1.calculating X^2 from synthetic distributions is that spatial

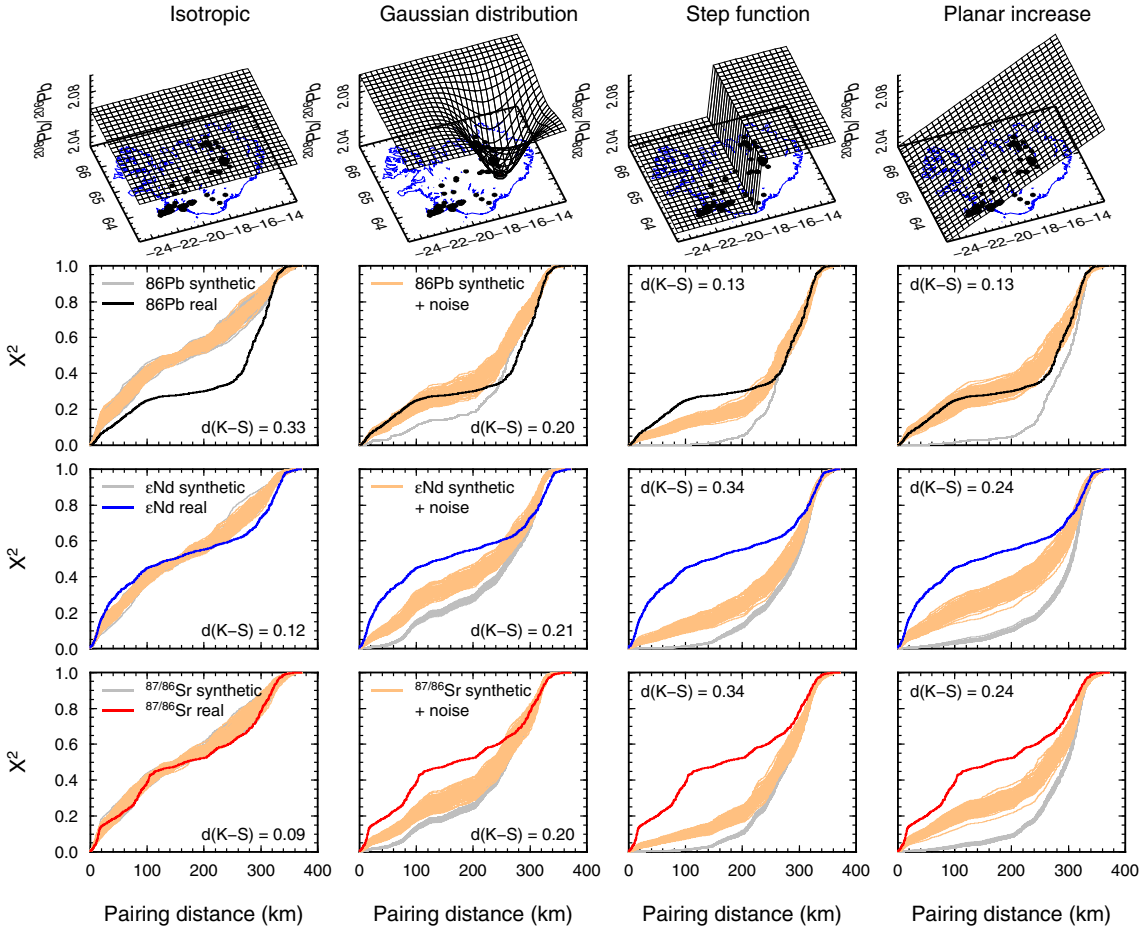

Fig. 12. Synthetic maps of $^{208}Pb/^{206}Pb$ (top), and the calculated cumulative chi-squared plots when these maps, and the equivalent maps for Nd and Sr isotopes, are sampled by the real sample distribution (second, third and fourth rows). Four synthetic maps of geochemistry are explored: a model in which the isotopic composition is the same across Iceland (set at the mean isotopic value, top left), a model where geochemistry varies according to a Gaussian anomaly (bandwidth 50 km, centred at −16.5 E 64.6 N), a model where there is a step change in isotopic composition at −19°E, and a model where the isotopic composition varies linearly east to west across the island (top right). The real spatial distribution of samples used in picking values from the synthetic maps are shown as black dots, only data from the neovolcanic zones (REP, WVZ, EVZ, SNVZ and NNVZ) are used. Two different calculations were performed using the synthetic profiles: In the first calculation, the synthetic profiles were sampled by the data, with the picked value perturbed by the analytical precision associated with each sample location. In the second calculation, the same sampling of the synthetic profiles occurs, only this time the perturbation of the selected values is greater—variability is scaled so that 40% of the total range in compositions is within 1 sigma of the mean value at that location. For both types of calculation the cumulative chi-squared plots were calculated 100 times. The resulting cumulative chi-squared distributions are drawn as thin grey lines for the first calculation type and orange lines for the second calculation type. The cumulative chi-squared from the real data are shown for reference as a black, blue or red line (Pb, Nd, Sr respectively). In each plot the Kolmogorov–Smirnov statistic d(K–S) has been calculated (Press et al., 1992), comparing the real chi-squared distribution and mean of the synthetic distribution with added noise (second type of calculation): d(K–S) is smallest when the profiles are most similar. In selecting the location of the Gaussian anomaly (top middle), a minimisation routine was used to minimising d(K–S) between the synthetic and real profiles for $^{208}Pb/^{206}Pb$, with the added constraint that the centre of the Gaussian anomaly must be in a plausible plume centre location (Shorttle et al., 2010).

distributions that create too much or too little local variance can be excluded. The synthetic spatial profiles in Fig. 12 show that a uniformly-heterogeneous spatial distribution cannot match the Pb isotopes and nor can a Gaussian anomaly. So there is evidence for a non-radially-symmetric chemical structure within the Icelandic mantle evidenced only in the Pb isotopes. To distinguish between a step change and planar increase we need to use the observation that differences were found in mean Pb isotopic composition and Pb mixing arrays between each of the NNVZ, SNVZ/EVZ, and REP/WVZ. In the simple step function model in Fig. 12 all three neovolcanic zones cannot be different, suggesting instead a progressive shift in geochemical parameters across Iceland and that the real structure is closest to the planar increase model.

8. SPATIAL STRUCTURE ON A 1000 km SCALE

Long wavelength positive free air gravity anomalies and broad regions of low seismic velocity indicate radial dispersal of the Iceland plume over distances of 1000–2000 km (Jones et al., 2002; Rickers et al., 2013). The spreading centres north and south of Iceland provide a linear sample of the laterally outflowing plume material, recording a spatial structure complementary to what we observe on Iceland. In this section we use principal component analysis of the combined Pb isotopic data from Iceland and the adjacent mid-ocean ridges to track the dispersal of the spatial structure we have recorded on Iceland into the North Atlantic mantle. Specifically, we want to understand how shifts in mean Pb isotopic composition and binary mixing array vary away from Iceland.

8.1. The Pb principal components of the North Atlantic mantle

Principal components on a combined Pb isotope dataset from Iceland, the Reykjanes, Kolbeinsey, Mohns and Knipovich Ridges have been calculated, normalising the data to ^{206}Pb. To provide a link with our previous analysis, it is first helpful to understand how the principal components calculated on the large regional dataset represent the Icelandic Pb isotope data. In Fig. 13a, data is projected onto the first two principal components (PC1 and PC2), which between them describe 99.9% of the total variance in the dataset. Data from Iceland forms a sigmoidal pattern in Fig. 13a: the SNFS and sEVZ flank zones have low PC1 and negative PC2, contiguous with the most radiogenic basalts from the WVZ/REP. However, the WVZ/REP data array trends from negative PC1 and PC2 to positive PC1 and PC2, where it intersects a cluster of points representing the data from central Iceland and the most radiogenic basalts from the NNVZ. The data array from the NNVZ is then sub-parallel to PC1, with most basalts having PC2 ≥ 0. The spatial structure we described on Iceland in terms of mean composition and binary mixing array is reproduced by principal component analysis. The increasingly positive PC1 in basalts from the REP to NNVZ in Fig. 13a, reflects the changing mean composition towards less radiogenic compositions (e.g. Fig. 5). PC2 then corresponds to a shift in the binary mixing array basalts fall along, with the differences being driven by the thoranogenic ^{208}Pb (e.g. the analysis in Fig. 8). Therefore, two principal components are required to describe the Pb isotope spatial structure on Iceland and we will next asses the distribution of these more broadly in the North Atlantic.

The work of Thirlwall (1995), Hanan and Schilling (1997), Schilling et al. (1999), Hanan et al. (2000), Blichert-Toft et al. (2005) has identified spatial differences in the Pb isotopic composition of basalts erupted along the MAR. Using principal components almost parallel to those in Fig. 13, (Blichert-Toft et al., 2005) divided the North Atlantic mantle into three geochemical provinces: (1) south of Iceland the Reykjanes Ridge samples mantle with initially low PC1, but which increases southwards along-ridge. (2) Immediately north of Iceland the Kolbeinsey Ridge has high and roughly constant PC1, and a smooth gradient of decreasing PC2 northwards. (3) North of Jan Mayen Island the MAR steps east to form the Mohns and Knipovich ridges, the basalts erupted here exhibit elevated PC2 and a gradient of increasing PC1 northwards. So the same elements of changing mean isotopic composition and binary mixing array are present in the adjacent ridges as in Iceland. However, Fig. 13a shows that the spatial structure on Iceland is not simply mapped into the adjacent ridges. The Kolbeinsey ridge does have a similar elevated PC1 (unradiogenic Pb) as north Iceland, but PC2 drops along-ridge to below that observed in the NNVZ. Purely in terms of Pb isotopes, the Mohns and Knipovich ridges appear more similar to north Iceland as they have similar elevated PC2 values, and PC1 compositions extending through NNVZ array to lower values. Along the Reykjanes Ridge and on-land Iceland in the SNFS and sEVZ flank zones, erupted basalts have PC2 $\leqslant 0$ over a wide range of PC1. The WVZ and REP basalts from Iceland are unique in Fig. 13a, in crossing from PC2 < 0 to PC2 > 0 whilst simultaneously increasing in PC1.

Another way to visualise the spatial systematics of the principal components is to map the data. In Fig. 13b and c we have mapped Icelandic and submarine ridge data, colouring samples by their principal component score. A complex spatial distribution of Pb isotope compositions emerges from Fig. 13b and c. Neither north nor south Iceland are compositionally contiguous with the adjacent ridges: in north Iceland PC1 decreases sharply going from subaerial to submarine basalts, whilst in south Iceland PC2 undergoes a step change at the coast. The scale of variability is also markedly different between subaerial and submarine portions of ridge. For the 500 km the MAR is subaerial on Iceland, PC1 and PC2 vary between the extremes seen over the entire $\sim$ 3000 km of submarine ridge. Different scales of spatial variability could be partly attributed to a low resolution and bias of sampling along the submarine ridges, because of which it is not generally possible to resolve structure on $<$ 100 km length scales. But the presence of high frequency variability should manifest as scatter of along-ridge isotopic compositions. That the differences between submarine and subaerial ridges in Fig. 13 are both

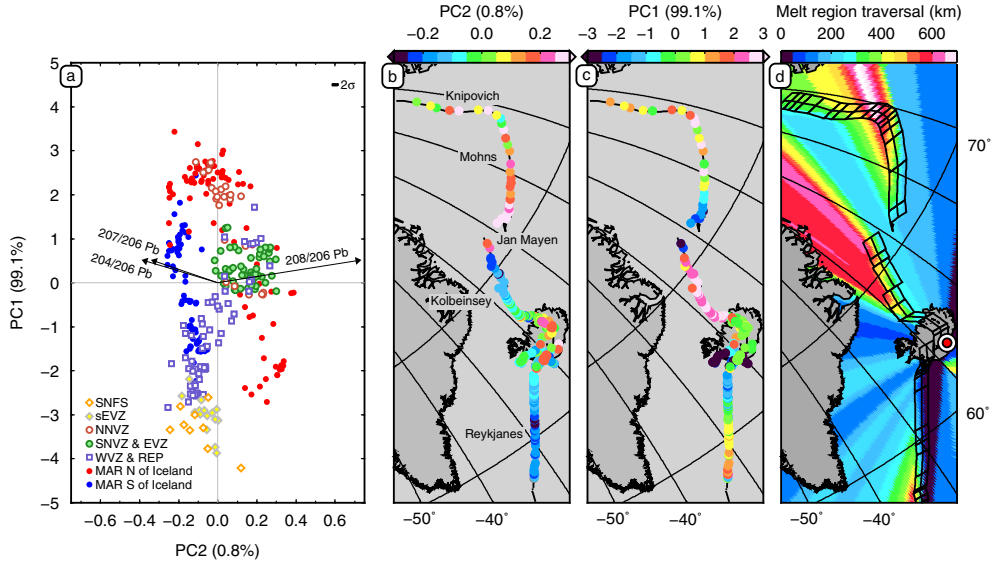

Fig. 13. Along-ridge maps of Pb isotopic composition projected into principal component space. The principal components calculated here are very similar to those of Blichert-Toft et al. (2005), but are from a larger dataset. PC1 represents a radiogenic–unradiogenic vector and PC2 is sensitive to the array data fall along. (a) Data projected onto the PC1–PC2 plane and coloured by geographic location. PC2 divides samples into groups from the ridges north and south of Iceland, with data from the WVZ of subaerial Iceland crossing this divide. Maps of data in (b) and (c) colour the samples by PC1 and PC2 respectively. (d) Map of the sub-ridge melt region distance traversed by a parcel of plume mantle reaching a given location (Shorttle et al., 2010). The melt region base was assumed to be 120 km in width, the outline of which is marked on the map. Melt region locations were calculated using the Euler poles of DeMets et al. (1994) and all distances were calculated for a spherical Earth. Data sources for ridge samples are Schilling et al. (1999), Thirlwall et al. (2004), Blichert-Toft et al. (2005), Peate et al. (2009).

large magnitude and spatially coherent makes it likely that real geochemical spatial structure is being mapped.

8.2. Mapping plume–ridge interaction

It is important to understand whether process, rather than intrinsic source differences, could be accounting for some of the structure observed along the submarine ridges. Shorttle et al. (2010) developed a model in which the greater depletion (i.e. unradiogenic $^{87}Sr/^{86}Sr$, low incompatible trace element ratios) of basalts erupted along the Kolbeinsey ridge compared with the Reykjanes Ridge, could be explained by progressive melting of laterally flowing plume material at the base of spreading centre melt regions. The effect of deep, small-degree partial melting would be to preferentially extract the most enriched and fusible lithologies from the mantle, leading to shifts in both the isotopic and trace element composition of the source (Shorttle et al., 2010). Here we assess the role of partial melting during plume outflow in generating spatial structure.

In Fig. 13d we have calculated a map of lateral melt region traversal distance. Fig. 13d indicates that the mantle reaching the Kolbeinsey and Knipovich ridges will have flowed further under spreading centres—allowing more opportunity for partial melting and depletion in the enriched components—than material flowing south to the Reykjanes Ridge. The patterns in Fig. 13d are very similar to those seen in PC1. The model also predicts the spike in enrichment at the Jan Mayen Fracture Zone followed by progressive depletion towards the Mohns–Knipovich intersection. Plume–ridge interaction is therefore one means by which spatial structure can be ingrown in outflowing plume material, turning an initially uniformly-heterogeneous source into one with radial asymmetry. Partial melting during outflow could also be used to explain the relative depletions of north and south Iceland, if partial melting of northward-bound plume occurred beneath the southern EVZ, whilst WVZ, REP and Reykjanes Ridge mantle avoided this. However, we know that spatial structure is not being created on Iceland in either Nd or Sr isotopes, so for Pb isotopes to be particularly sensitive to processing during outflow the radiogenic Pb would have to reside in a low solidus phase that had little leverage on Sr or Nd isotopic compositions. It is not clear what phase could meet these criteria, so it is unlikely that depletion on Iceland is being ingrown by progressive melting during outflow. If partial melting during outflow only manifests over large distances, then spatial structure could be decoupled on the $>$ 1000 km scale from that on the $<$ 500 km scale.

Unlike ridge scale structure in PC1, PC2 is clearly different from the map of melt region traversal distances (compare Fig. 13b and d). Progressive depletion of the source is unable to generate changes in binary mixing array in the simple two lithology model explored by Shorttle et al., 2010. However, if the enriched endmember controlling the gradient in Pb–Pb isotope space were itself a mixture of multiple real mantle components with distinct lithologies and melting properties, then changes in the relative abundance of these endmembers would affect the gradient of mixing regressions. If the partial melting process occurring during outflow were able to preferentially extract not only melts from enriched lithologies, but also discriminate between

the multiple enriched lithologies, (pseudo-) binary mixing arrays could be altered. However, two observations indicate that partial melting during outflow cannot be controlling array structure in any simple way. Firstly, progressive depletion along the Reykjanes Ridge occurs independently of shifts in PC2. Secondly, the Kolbeinsey ridge basalts have roughly constant unradiogenic Pb compositions (PC1), but their PC2 changes progressively along the ridge (Fig. 13). Therefore, if processes are creating changes in array and mean composition, they are not acting in the same way north and south of Iceland. There may be dynamical reasons for the processes involved in plume–ridge interaction to vary non-radially symmetrically around Iceland—e.g. the northward reduction in spreading rate along the MAR, or the less oblique spreading of the Kolbeinsey ridge compared with the Reykjanes Ridge. But our finding of spatial structure in the mantle beneath Iceland hints that source characteristics could be acting independent of process, or convolved with it, to generate large-scale structure in North Atlantic basalt chemistry.

To summarise this section, the spatial structure on Iceland does not simply map into the chemistry of adjacent spreading centres. The north–centre–south gradient in Pb isotopes seen on Iceland does initially appear to extrapolate to the adjacent ridges, with the Kolbeinsey and Reykjanes Ridge basalts showing unradiogenic and radiogenic compositions respectively. Partial melting of outflowing material could explain a large part of this PC1 structure, with the mantle reaching southwest Iceland and the Reykjanes Ridge having experienced less melt extraction than that flowing northwards beneath Iceland's northern volcanic zones to the Kolbeinsey ridge. Intrinsic north–south depletion seen on Iceland may then be superimposed upon the physical process of progressive melt extraction to create large scale structure in PC1 (Fig. 13c). However, the distribution of PC2 does not fit easily into such a model. The gradual north–south shift in the binary mixing array each volcanic zone defines on Iceland breaks down north of Iceland, as the Kolbeinsey ridge PC2 varies systematically northwards back towards values similar to those seen on the Reykjanes Ridge. It is not clear what physical process could generate this along-ridge gradient in PC2, so we are left to assume it is an intrinsic feature of the source being mapped into ridge basalt chemistry (Blichert-Toft et al., 2005). PC2 therefore suggests that the North Atlantic mantle is highly provincial in its isotopic character. Iceland itself is a centre of isotopic provincialism, with the WVZ unique in having coupled variation of PC1 and PC2.

9. DISCUSSION

By representing diverse spatial observations with a common metric, their cumulative chi-squared distributions, we have demonstrated that there is significant spatial structure in Pb isotopic composition recorded in Iceland's rift zone basalts. At 100 km sample pairing distance, the Pb isotopic composition of basalts still reflects the local flavour of end-member melts and their mixing proportions. This is in contrast to Sr and Nd isotope systems, for which basalts do not exhibit compositional provincialism. Pb isotopes therefore have longer range spatial structure than Sr or Nd isotopes and are decoupled from them on length scales similar to neovolcanic zones. Combining the spatial observations with synthetic spatial geochemical profiles indicates that the Pb isotopes are more consistent with a continuous shift in compositions in the Icelandic mantle than a bilateral asymmetry, Gaussian anomaly or a uniformly-heterogeneous distribution. A more subtle result is that thoranogenic ^{208}Pb defines a spatial structure in the Pb isotope regression parameters that is complementary to that seen in mean Pb isotopic composition.

Here we explore three topics with general relevance to the interpretation of the geochemical structure at ocean islands and mid-ocean ridges, (1) the role of tectonic segmentation in creating geochemical provincialism; (2) possible origins of the diverse Pb isotopic composition of basalts erupted in the North Atlantic; and (3) the implications of our results for the interpretation of bilateral asymmetry in plume conduits.

9.1. The control of tectonics on geochemical spatial structure

The fundamental unit of rift segmentation on Iceland is the volcanic system (Jóhannesson and Smundsson, 2009). These units are defined by en echelon fissures, that in many cases are also accompanied by central volcanoes. The individual coloured polygons mapped in Fig. 2a are a coarse representation of Iceland's currently active volcanic systems. Ideally, we would have grouped samples according to this structural unit, but there is not enough data yet available to make this practical. Instead, we have grouped the individual volcanic systems into what we describe as neovolcanic 'zones', defined both by large-scale tectonic segmentation of the axial rift (e.g. the step from the WVZ to the SNVZ) and the geochemical composition of basalts erupted. So it is not entirely surprising that in Sections 4 and 5 we found systematic differences between the geochemistry of the grouped datasets. The circularity of this approach justifies examining the data explicitly in the spatial domain, where locational information is purely a sample's longitude and latitude.

The $\sim$ 130 km length scale of coupled Sr–Nd–Pb isotope systematics, obtained from spatial statistical analysis, indicates that grouping samples by neovolcanic zone roughly describes the first-order geochemical segmentation on Iceland. To test the physical significance of this length scale further will require more focused studies on spatially and temporally restricted sample sets. In particular, with existing isotope data it is difficult to resolve how alike adjacent volcanic systems are and whether they show similar differences in mean Pb isotope composition and mixing array as do the neovolcanic zones. Although, that it is possible to see large scale coherent spatial structure means it is unlikely that inter-system variation is as high amplitude as inter-zone variation.

Developing a better understanding of volcanic systems will be important for explaining why Pb, Sr and Nd isotopes are coherent on a local scale ($<$ 140 km). In the model of Rudge et al. (2013), incomplete mixing of melts from a single melting region gives rise to correlations in Pb–Sr–

Nd isotopes. The observed 130–150 km length scale of Sr–Nd–Pb correlation on Iceland could therefore represent the distance over which communication between melts occurs in the crust and/or mantle, an information length scale effectively delimiting a melting region. In this model, volcanic systems could be directly controlling the expression of mantle geochemical structure. Alternatively, 130–150 km could be the distance over which the mantle melting processes and source remain relatively constant—if, for example, the mantle exhibits an E–W shift in composition (Fig. 12), then the approximate north–south trend of the volcanic systems will naturally produce basalts of the same composition over much of their length.

Another important, but poorly constrained, parameter for understanding how basalt chemistry maps back into the mantle, is the amount of lateral transport of melt. If material is transported and mixed along strike of a neovolcanic zone, then gradational changes in mantle composition will appear discretised. It seems unlikely that the north of the WVZ can know about the melts supplied at its southern end over 80 km away. However, the volcanic systems that constitute the neovolcanic zones are on the scale of tens of km and could more plausibly be supplying melt laterally from a central location of storage and homogenisation (Björnsson et al., 1977). More generally, what we need to know is how deep the surface segmentation into volcanic systems extends down into the crust and mantle. It is possible that in the lower crust or upper mantle, along-strike transport of melt is occurring over very different distances than the few tens of km implied by upper crustal tectonics. Magma transport in the crust and mantle may therefore impose a minimum length scale of compositional structure that is resolvable by analysis of basalts. Gaining a greater understanding of magma transport mechanisms will be a key step towards interpreting basalt chemistry in terms of mantle structure.

9.2. The origin of Pb isotope diversity

To understand the origins of Pb isotope diversity in the North Atlantic it is necessary to explore the possible roles of source and process in generating the observed patterns—allowing that the importance of each of these may be different between creating shifts in binary mixing array and shifts is mean composition.

In Section 8 we showed that one way to create structure in PC1 (essentially a radiogenic—un-radiogenic vector) was by partial melting of a heterogeneous mantle during plume outflow. However, a key constraint for physical models generating spatial structure on subaerial Iceland, is the decoupling between Pb and Sr/Nd isotope systems occurring on length scales > 130 km. This decoupling rules out a simple change in the abundance of enriched material across Iceland, as suggested for the regional scale pattern of PC1 in our model, as having more or less enriched material should also influence the Sr and Nd isotopic compositions of basalts (which although not observed on Iceland, is seen on a regional scale (Shorttle et al., 2010)). Any mechanism for decoupling must also only act between neovolcanic zones, so that correlation between Pb, Sr, and Nd can be maintained at a local level.

It is difficult to envisage process occurring during melting under Iceland today that could strongly separate Pb systematics from those of Sr and Nd, without there already being intrinsic differences in source. One possibility is that there are multiple enriched components beneath Iceland, with similar Sr and Nd isotope characteristics, but different Pb isotopic compositions. This scenario would invoke a mantle like that proposed by Hanan et al. (2000), Thirlwall et al. (2004), where melts from a common depleted component (ID1 in the case of Thirlwall et al. (2004)) can mix with melts from an enriched lithology mixture (IE1—IE2 of Thirlwall et al. (2004)), the exact makeup of which varies progressively across Iceland. Such a scenario appears to work for Pb–Sr/Nd arrays (Fig. 7) and Sr–Nd arrays (Fig. 6), both of which could be interpreted as converging at high ϵNd and low $^{208}Pb/^{204}Pb$ whilst diverging at the enriched end. For Pb isotope systematics however, the mixing of melts from three components cannot so simply create the observed arrays. Although a three component mantle offers enough flexibility to describe all the Pb isotope variability (as indicated by the PCs in Fig. 13), it raises the question of how melts from these components are physically interacting to create the range of pseudo-endmembers necessary: because a key observation is that irrespective of how many components are present in the mantle beneath Iceland, the melts from each zone form coherent binary mixing arrays that require only two endmembers to be present locally. What this observation indicates is that mixing in the mantle or crust must be key in creating the apparent isotopic identity of endmember melts for each zone.

Without knowing the lithological character of the components beneath Iceland, it is difficult to predict how mixing might occur during melting to produce the binary mixing arrays. Shorttle and Maclennan (2011), using the major element compositions of basalts, identified the presence of two lithologies in the Icelandic mantle: a normal KLB-1 type peridotite, and a peridotite refertilised by up to 50% recycled MORB. Such lithological range could host unradiogenic Pb in the peridotite and radiogenic Pb in a high U/Pb recycled basalt. However, isotope systematics clearly demand more variability than just two sources, and it is difficult to see direct evidence for the lithological character of these. Specifically, the high Th/U signature represented by basalts from central and northern Iceland, the Mohns, Knipovich and the southern Kolbeinsey ridge (Blichert-Toft et al., 2005), is a subtle shift in the slopes of Pb isotope arrays that may be difficult to observe in major element chemistry. The systematics of how this high Th/U component (PC2 in Fig. 13) is distributed and entering melts is also difficult to understand. This is because of its contrasting behaviour between The Kolbeinsey ridge, where PC2 decreases along ridge at nearly constant unradiogenic PC1, and the WVZ/REP, where both PC1 and PC2 covary (Fig. 13).

In summary, we acknowledge that published models can explain the range of isotopic compositions observed in the North Atlantic (e.g. Hanan et al., 2000; Thirlwall et al., 2004). However, these models and our own under-

standing are far from having a physical and causal explanation of how source and process are creating all isotopic provincialism in the North Atlantic. One step towards simplifying the interpretation of along-ridge geochemistry may be to allow that plume material is partially melting as it outflows.

9.3. Bilateral geochemical asymmetry in plume conduits

On Iceland, where the neovolcanic zones provide laterally extensive sampling of the mantle, it is possible to identify staggered yet progressive shifts in geochemical parameters between zones. However, spatial structure can only be resolved down to the unit volume of mantle that a given volcano/ridge segment is in communication with. Without knowing the extent of ridge parallel magma transport and mixing it is therefore not possible to map geochemical parameters at the surface directly into mantle compositional structure. Because of this we can assume that the 140 km length scale at which decoupling between Sr, Nd, and Pb becomes apparent is a maximum for the true dimension of changes in mantle structure. For locations where spatial sampling is discontinuous it is going to be even more difficult than on Iceland to resolve real spatial structure (as shown in the cartoon of Fig. 1). For parallel chains of volcanoes such as Hawaii, where eruptions occur at discrete pairs of volcanic edifices (belonging to either the Loa or Kea chain) (Abouchami et al., 2005; Weis et al., 2011), there will always be the propensity to see dichotomous geochemical relationships regardless of the underlying mantle chemical structure. Most ocean islands do not provide sufficient spatial resolution for true bilateral asymmetry to be identified. Chemical differences between chains of ocean island volcanoes should at most be interpreted as evidence for laterally non-uniformly-heterogeneous mantle structure. To confidently resolve bilateral asymmetry of the type proposed by Abouchami et al. (2005), Huang et al. (2011), Weis et al. (2011) would require sampling of the mantle at many more locations away from the plume axis.

Separating source from process is a fundamental problem in geochemistry. Contrasting hypotheses have recently been presented for how bilateral compositional spatial structure in Hawaiian basalts can be created—Weis et al. (2011) by source and Ballmer et al. (2011) by process. The case of Hawaiian compositional structure is a typical example of how geochemical observations can be explained by a number of models along the source–process spectrum. Sampling the mantle through basalt chemistry will always mean that process is a large part of any compositional signal. However, the real difficulty is not the amount of process, but that the processes involved in melting and extraction are themselves poorly understood. A lithologically heterogeneous mantle adds extra complexity to the system, as the melting now involves multiple solidi and greater solid–liquid disequilibrium. Without properly understanding one or the other of source and process, identifying mantle compositional structure will always be an underconstrained problem.

10. CONCLUSIONS

1. Grouping samples by the neovolcanic zone they are erupted from, we identify statistically significant differences in the mean Pb isotopic composition and Pb–Sr and Pb–Nd binary mixing arrays between neovolcanic zones. There is a shift south to north across Iceland where the basalts have progressively more depleted Pb isotopic compositions and the binary mixing array they lie on shifts to higher $^{208}Pb/^{206}Pb$ at a given $^{207}Pb/^{206}Pb$. Neither Sr nor Nd isotopes show the same systematic offsets in mean composition or binary mixing array between neovolcanic zones as seen in the Pb isotopes.
2. The Pb isotopic composition of a basalt is more sensitive to location than either its Sr or Nd isotopic composition. On an island-scale, the different strengths of positive spatial autocorrelation for Pb, Sr, and Nd isotopes are outside what can be explained by the lower signal to noise of Sr and Nd isotope systems. Within individual neovolcanic zones, spatial autocorrelation is similar between Sr, Nd, and Pb isotopes. On short length scales Pb, Sr, and Nd isotopes exhibit correlated behaviour.
3. Changes in Pb isotope arrays occur progressively as the neovolcanic zones are stepped through from south to north. Local regressions become increasingly different from one another as the data groupings are further apart. Spatial structure in Pb isotope binary mixing arrays is created by different amounts of thoranogenic ^{208}Pb in the mantle sources.
4. Cumulative chi-squared plots are a means of representing diverse spatial observations by a single metric. Considering the data in terms of cumulative chi-squared allows direct comparison between independent observations, significance testing against null hypothesis distributions, and comparison with synthetic spatial distributions. Cumulative chi-squared plots show that Sr, Nd and Pb isotope systems are coupled within Iceland on length scales < 130 km, but decoupled over greater distances.
5. Combining the analysis of synthetic spatial distributions of geochemistry with the observations of progressively shifting local structure, indicates that a progressive increase in the average level of mantle depletion is a better match to the Pb isotope cumulative chi-squared distributions than either uniformly-heterogeneous, Gaussian, or step change spatial profiles. By contrast Sr and Nd cumulative chi-squared profiles are best matched by uniformly-heterogeneous chemical distributions.
6. Spatial structure in Pb isotopes exists over several thousand km in the North Atlantic mantle. The geochemical spatial structure found along the ridges adjacent to Iceland is present within Iceland's neovolcanic zones. The part of the variation reflecting greater or lesser depletion (PC1) can be explained on large lengthscales by partial melting during outflow of the plume head material. The shifts in $^{208}Pb/^{206}Pb$ at a given $^{207}Pb/^{206}Pb$ (PC2) however, cannot be easily explained by this same process. Nor is the structure in PC2 throughout the North Atlantic the simple result of the lateral advection of the spatial structure we observe on subaerial Iceland.

7. The complexity of geochemical spatial structure on Iceland, where spatial sampling of the mantle is extensive, implies that the bilateral asymmetry in plume conduits inferred in other ocean island settings, where sampling of the mantle is spatially restricted, cannot be reliably identified. Having only a few discrete volcanic edifices focusing and mixing melts will necessarily create compositional dichotomies across islands.

ACKNOWLEDGEMENTS

Jason Day helped greatly with MC-ICP-MS and ICP-MS work. Nick Odling and Godfrey Fitton are thanked for their assistance with the XRF analyses. Ben Winpenny and Margaret Hartley kindly provided material from Svartadyngja. Hazel Chapman helped with Sr chemistry and ran the TIMS. David Neave, Ben Dubacq, Margaret Hartley and Sally Gibson are thanked for their readings of the early drafts. David Wilson provided valuable discussion on chemical separation, analysis and correction methodology for Pb isotopes. The reviewers and editor are thanked for their great efforts to improve the clarity of the manuscript.

APPENDIX A. EFFICACY OF TL MASS FRACTIONATION CORRECTION FOR PB ISOTOPES

The premise of correcting for mass fractionation with Tl spiking is that isotopes of Pb and Tl will experience the same amount of mass dependent fractionation during analysis (i.e. will have the same fractionation factor). Therefore, by spiking a sample with a Tl solution of known $^{205}Tl/^{203}Tl$ and monitoring the 205 and 203 beams during analysis, the known fractionation of the Tl isotopes can be used to correct for the unknown fractionation experienced by the Pb isotopes. The logic of this approach can be seen from the exponential correction law (White et al., 2000),

$$\left(\frac{^{208}Pb}{^{206}Pb}\right)_t = \left(\frac{^{208}Pb}{^{206}Pb}\right)_m \left[\frac{M^{Pb}_{208}}{M^{Pb}_{206}}\right]^f, \quad (A.1)$$

where f is the fractionation coefficient and subscripts t and m refer to true and measured values respectively. To obtain $(^{208}Pb/^{206}Pb)_t$, all that needs to be known is f_{Pb}. However, with no stable isotope pair, Pb isotopes require some other means of tracking mass fractionation. Reformulating Eq. A.1 for Tl,

$$\left(\frac{^{205}Tl}{^{203}Tl}\right)_t = \left(\frac{^{205}Tl}{^{203}Tl}\right)_m \left[\frac{M^{Tl}_{205}}{M^{Tl}_{203}}\right]^f, \quad (A.2)$$

shows that spiking with an element of similar mass range and known isotopic composition ($(^{205}Tl/^{203}Tl)_t$) could allow for the calculation of f. Dividing Eq. A.1 by A.2 and rearranging obtains the relationship for the slope,

$$S = \frac{f_{Pb}}{f_{Tl}} \frac{ln(M^{Pb}_{208}/M^{Pb}_{206})}{ln(M^{Tl}_{205}/M^{Tl}_{203})} \quad (A.3)$$

where the slope is the gradient of a regression line through the raw analyses in $\ln(^{208}Pb/^{206}Pb)$ vs. $\ln(^{205}Tl/^{203}Tl)$ space (White et al., 2000). Eq. A.3 allows for the assumption of $f_{Tl} = f_{Pb}$ to be tested, by plotting the uncorrected analyses of a given solution run repeatedly throughout an analytical session. If $f_{Tl}/f_{Pb} = 1$ then $S = 0.98553$, slopes of different gradient occur when $f_{Tl}/f_{Pb} = K$ where the constant $K \neq 1$, if $f_{Tl}/f_{Pb} \neq K$ then the data will scatter. The caveat to this approach is that the more stable the mass fractionation in a session, the more poorly defined S becomes. The effect of instrument stability on S can be seen in Fig. A.1a, where the raw in-run NIST SRM-981 standard values are plotted. The data from FL04 and HBT10-1g runs

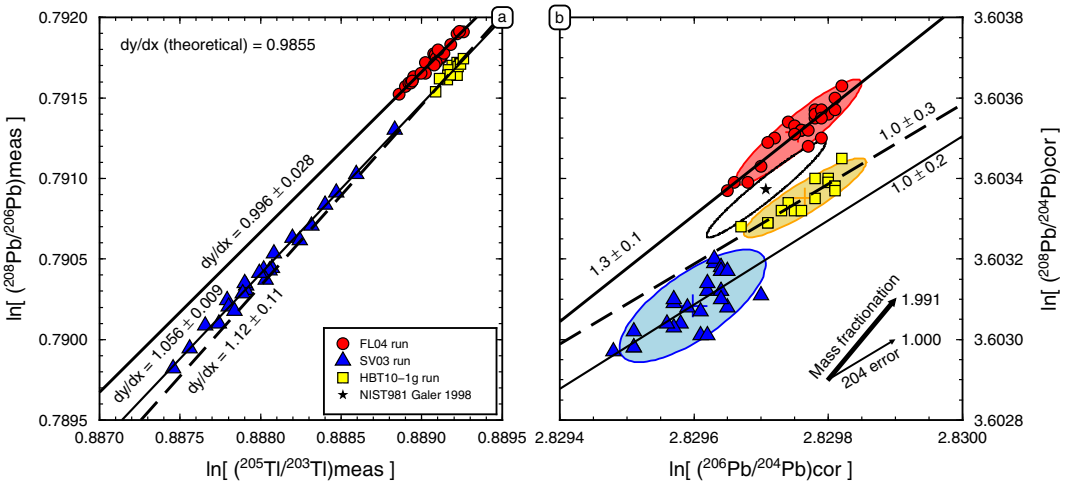

Fig. A.1. Analyses of NIST SRM-981 from this study's three analytical sessions. In (a) data are left un-corrected for mass fractionation so that the relative fractionation behaviour of Pb and Tl can be assessed. Regressions have been calculated using the method of York (1969) and errors on the gradient (dy/dx) are quoted at the 2σ level for comparison to the theoretic value for when $f_{Tl} = f_{Pb}$. In (b) the mass fractionation corrected data are plotted having assumed a $f_{Tl}/f_{Pb} = 1$. Regressions are fitted to the data to distinguish between residual uncorrected mass fractionation (slope = 1.991) and correlated shot noise (i.e. error on ^{204}Pb, slope = 1). The reference value of NIST SRM-981 as determined by Galer and Abouchami (1998), Abouchami et al. (2000) using TIMS triple spike is plotted for reference with a 2σ error ellipse. The 2σ error ellipses defining the external reproducibility of NIST SRM-981 run during this study are also shown as the blue red and yellow regions.

are clustered in the top right of the diagram, whilst data from SV03 spreads over five times the range. The unstable mass fractionation during the SV03 session means that the relative fractionation of Pb and Tl is well resolved. The slope defined by the SV03 session NIST SRM-981 standards has a value of $1.056 \pm 0.009, > 15\sigma$ away from the theoretical value. Fig. A.1a also shows that there is statistically significant deviation from the theoretical gradient for the HBT10-1g session. Only the FL04 session is within uncertainty of the theoretical gradient. Therefore, the fractionation of Pb and Tl in the mass spectrometer is not always equal and has changed at least once during the May 2010–October 2011 analytical period.

The mass fractionation corrected standard values are presented in Fig. A.1b, corrected assuming $f_{Tl}/f_{Pb} = 1$. Despite the assumption of $f_{Tl}/f_{Pb} = 1$ probably being wrong for at least two of the analytical sessions, all the data plots close to the triple spike TIMS analysis of NIST SRM-981 from Galer and Abouchami (1998). The efficacy of Tl spiking and the exponential law can be also be seen more generally by the collapse in variability of the SV03 standard analyses to a similarly tight cluster as the FL04 and HBT10-1g standards. If applying the exponential law fully described the mass fractionation then residual correlation in the corrected data should only be from shot noise in the minor 204 isotope, creating a data array with a gradient of 1 in $\ln[^{208}Pb/^{204}Pb]$ versus $\ln[^{206}Pb/^{204}Pb]$ space. Correlation arising purely from un-corrected mass fractionation in Fig. A.1b will have a slope of 1.991. The slopes of data in SV03 and HBT10-1g sessions are both within error of 1, suggesting that residual correlation is dominated counting statistics on ^{204}Pb. The FL04 session however, defines a line with steeper gradient (1.3 ± 0.1) significantly different from one. A small amount of uncorrected mass fractionation could therefore be present in the FL04 data, but at a level where 204 shot noise nonetheless dominates.

In summary, the NIST SRM-981 results in Fig. A.1 confirm that the correction method used in this study is effective in accounting for the mass fractionation experienced by pure sample solutions. The residual offset of standards from their nominal value after correction is overwhelmingly 204 shot noise, and the final linear correction onto the Galer and Abouchami (1998) value is very small. These residual effects are over an order of magnitude smaller than the differences between datasets we look at in this study and therefore don't affect our results.

APPENDIX B. SUPPLEMENTARY TABLES AND FIGURES

See Tables B.8, B.9, B.10.

APPENDIX C. QUANTIFYING THE SHAPE OF THE ISOTOPIC DISTRIBUTIONS FROM ICELAND'S NEOVOLCANIC ZONES

The shape and location of a univariate distribution is described by its moments. The first moment defines the mean, and subsequent moments about the mean describe the width of the distribution (or variance, second moment) and asymmetry (or skewness, third moment). The analytical uncertainty on each data point can be taken into account when calculating the moments by introducing a weighting term proportional to $1/\sigma^2$. The first three weighted moments and the median for each neovolcanic zone's 0distribution are given in Table B.8. Weighted means ($\hat{\mu}_1$)

Table B.7
List of data sources used in compiling isotopic analyses.

Reference	Number of samples			Method[a]
	Pb	Sr	Nd	
Brandon et al. (2007)	0	0	8	–/–/p
Breddam (2002)	0	4	4	t/t/t
Debaille et al. (2009)	0	14	9	–/p/p
Elliott et al. (1991)	0	5	7	–/t/t
Halldorsson et al. (2008)	15	20	16	p/p/p
Hémond et al. (1993)	0	31	32	–/t/t
Kempton et al. (2000)	0	13	13	–/t/t
Kokfelt et al. (2006)	43	42	43	t/t/t
Kokfelt et al. (2009)	5	5	5	t/t/t
Koornneef et al. (2012b)	0	0	33	–/–/p
Kuritani et al. (2011)	4	4	4	t/t/t
Lacasse et al. (2007)	0	1	1	–/t/t
Peate et al. (2009)	25	10	14	p/p/p
Peate et al. (2010)	29	10	10	p/p/p
Sigmarsson et al. (1992)	0	2	2	–/t/t
Sigmarsson et al. (2000)	0	1	0	–/t/–
Skovgaard et al. (2001)	0	0	12	–/–/t
Steinthorsson et al. (2000)	0	5	5	–/t/–
Stracke et al. (2003)	0	43	43	–/t/t
Thirlwall et al. (2004)	31	22	28	t/t/t
Thirlwall et al. (2006)	0	12	7	–/t/t
Total	152	244	296	–

[a] Method of analysis for Pb/Sr/Nd: t = TIMS, p = plasma.

Table B.8
The first three weighted moments and the weighted medians describing the geochemical distribution of the NNVZ, central Iceland and south western Iceland isotopic data.[a]

Zone	$\hat{\mu}_1$	$\tilde{x}$	$(\hat{\mu}_2)^{1/2}$	$\hat{\mu}_3$	N_d
	$^{206}Pb/^{204}Pb$				
NNVZ	18.13 (4)	18.09 (1)	0.19 (4)	0.8 (2)	24
SNVZ&EVZ	18.39 (9)	18.4 (1)	0.06 (4)	−0.5 (8)	68
REP&WVZ	18.66 (9)	18.7 (1)	0.21 (5)	−0.3 (2)	59
	$^{207}Pb/^{204}Pb$				
NNVZ	15.443 (6)	15.434 (4)	0.023 (6)	0.7 (1)	24
SNVZ&EVZ	15.47 (1)	15.47 (1)	0.011 (4)	−0.8 (0.5)	68
REP&WVZ	15.495 (9)	15.50 (1)	0.020 (3)	−0.6 (2)	59
	$^{208}Pb/^{204}Pb$				
NNVZ	37.84 (7)	37.73 (3)	0.26 (7)	0.7 (3)	24
SNVZ&EVZ	38.1 (1)	38.2 (2)	0.07 (7)	−1.3 (8)	68
REP&WVZ	38.27 (5)	38.25 (7)	0.16 (3)	−0.1 (0.5)	59
	$^{87}Sr/^{86}Sr$				
NNVZ	0.70303 (2)	0.70303 (3)	1.03e−04 (4)	0.0 (2)	67
SNVZ&EVZ	0.70323 (1)	0.70326 (1)	7.6e−05 (8)	−0.8 (4)	80
REP&WVZ	0.70308 (4)	0.70310 (4)	8.5e−05 (4)	−0.6 (1)	78
	ϵNd				
NNVZ	8.59 (5)	8.62 (9)	0.73 (5)	0.32 (9)	82
SNVZ&EVZ	7.6 (3)	7.8 (2)	0.8 (1)	−0.4 (3)	76
REP&WVZ	8.2 (1)	8.02 (9)	0.96 (4)	0.2 (2)	116

[a] $\hat{\mu}_1$ = weighted mean of distribution, $\tilde{x}$ = weighted median of distribution, $(\hat{\mu}_2)^{1/2}$ = weighted standard deviation and $\hat{\mu}_3$ = weighted skewness. One sigma errors in parentheses after each value are calculated from the jackknifing routine described in Section 2.3.3 and refer to uncertainty on the last digit. Weights used in determining parameters were calculated from quoted analytical uncertainty.

Table B.9
Binary mixing regression parameters calculated for NNVZ, SNVZ & EVZ, and REP & WVZ data for Figs. 6 and 7.[a]

Region	c	X_1	X_2	Y_1	Y_2	χ^2_r	p
	ϵNd vs. $^{87}Sr/^{86}Sr$						
NNVZ	0.97 (2)	0.70280 (1)	0.70328 (1)	10.2 (2)	7.0 (2)	0.9	0.00
SNVZ&EVZ	1.4 (1)	0.70294 (1)	0.70340 (1)	9.7 (2)	6.3 (3)	2.8	0.00
REP&WVZ	1.15 (2)	0.70286 (1)	0.70329 (2)	10.45 (6)	6.0 (2)	3.3	0.00
	ϵNd vs. Nb/Zr						
NNVZ	0.80 (1)	0.012 (1)	0.122 (2)	10.22 (9)	7.06 (5)	2.7	0.00
SNVZ&EVZ	1.15 (3)	0.024 (6)	0.156 (5)	10.1 (2)	6.1 (2)	1.2	0.00
REP&WVZ	0.71 (1)	0.003 (1)	0.204 (6)	10.16 (5)	6.4 (1)	3.6	0.00
	$^{208}Pb/^{204}Pb$ vs. $^{87}Sr/^{86}Sr$						
NNVZ	1.25 (2)	0.7028 (3)	0.7033 (1)	37.52 (7)	38.2 (1)	6.9	1
SNVZ&EVZ	1.3 (2)	0.70307 (4)	0.70336 (2)	37.91 (2)	38.31 (2)	18	0.00
REP&WVZ	1.0 (1)	0.70293 (3)	0.70322 (4)	37.81 (2)	38.62 (3)	11	0.00
	$^{208}Pb/^{204}Pb$ vs. ϵNd						
NNVZ	0.38 (8)	7.2 (2)	10.4 (3)	38.19 (9)	37.54 (4)	9.4	0.1
SNVZ&EVZ	0.8 (1)	7.1 (2)	9.02 (6)	38.32 (3)	37.92 (1)	3.4	0.00
REP&WVZ	1.5 (1)	6.1 (4)	10.6 (2)	38.62 (2)	37.82 (1)	14	0.00
	$^{208}Pb/^{204}Pb$ vs. Nb/Zr						
NNVZ	1.3 (5)	0.005 (8)	0.122 (3)	37.4 (1)	38.4 (2)	9.0	0.00
SNVZ&EVZ	0.9 (1)	0.047 (7)	0.135 (6)	37.86 (3)	38.32 (3)	4.7	0.00
REP&WVZ	0.26 (6)	0.005 (9)	0.23 (1)	37.81 (2)	38.58 (2)	19	0.00

[a] Quoted parameters fulfil the general equation for binary mixing: $Ax + Bxy + Cy + D = 0$, where $A = Y_2 - Y_1c$, $B = c - 1$, $C = X_1 - X_2c$ and $D = Y_1X_2c - Y_2X_1$, with X_i and Y_i as the respective x and y axis ratios for the i^{th} component. The curvature of the hyperbola is defined by the concentration ratio $c = (a_1/b_1)/(a_2/b_2)$, where a_i is the concentration of the denominator of Y_i and b_i is the concentration of the denominator of X_i (Sohn, 2005). Regression parameters calculated using maximum likelihood estimation code of Sohn (2005), with errors determined by Jackknifing and quoted in parentheses at the 1σ level on the last digit. p-values are determined using the F-test and are percentage probabilities of the null hypothesis being true, that the data are better fitted by a random Gaussian distribution than binary mixing.

for the NNVZ and REP/WVZ are consistently different for Pb isotopes outside the 1σ calculated from jackknifing. Central Iceland Pb isotope means are intermediate between the northern and southern zones, creating a pattern of

Table B.10
Linear regression parameters in Pb–Pb space for the data plotted in Fig. 8.[a]

Zone	$^{204}Pb/^{206}Pb$ vs. $^{207}Pb/^{206}Pb$					$^{204}Pb/^{206}Pb$ vs. $^{208}Pb/^{206}Pb$					$^{207}Pb/^{206}Pb$ vs. $^{208}Pb/^{206}Pb$				
	m	c	χ^2_r	R^2	p	m	c	χ^2_r	R^2	p	m	c	χ^2_r	R^2	p
NNVZ	0.0740 (3)	−0.0078 (2)	16	1.00	0.00	0.0602 (3)	−0.070 (1)	205	0.98	0.00	0.816 (2)	−0.850 (4)	331	0.99	0.00
SNVZ&EVZ	0.0689 (3)	−0.0036 (3)	97	0.96	0.00	0.0421 (3)	−0.033 (1)	769	0.75	0.00	0.689 (2)	−0.587 (5)	1050	0.88	0.00
REP&WVZ	0.0710 (1)	−0.0054 (1)	86	1.00	0.00	0.0401 (1)	−0.0288 (2)	353	0.99	0.00	0.560 (1)	−0.319 (1)	575	0.99	0.00
sEVZ	0.066 (1)	−0.001 (1)	16	0.98	0.00	0.046 (1)	−0.041 (2)	321	0.77	3	0.643 (9)	−0.488 (18)	527	0.85	1
Snæfellsnes	0.072 (1)	−0.006 (1)	28	0.97	0.00	0.054 (1)	−0.057 (2)	94	0.93	0.00	0.766 (6)	−0.739 (13)	108	0.98	0.00

[a] The regression gradient is m, the y-intercept c, the reduced chi-squared for each regression is χ^2_r, and the proportion of variance explained by the regression model is the R^2 value. We have defined $R^2 = 1 - (\chi^2 df_0)/(\chi^2_0 df)$, where χ^2 is the chi-squared value minimised in the York (1969) regression, χ^2_0 is the chi-squared for a model where the gradient is zero (i.e. no correlation between x and y), and df and df_0 represent the degrees of freedom in the model case ($df = N_d - 2$) and the no correlation case ($df = N_d - 1$) respectively. *p*-values are estimated using an F-test against a model with zero gradient and are quoted as percentages. Errors in parentheses are given at the 1σ level and for NNVZ, SNVZ&EVZ and REP&WVZ are calculated by the jackknifing routine described in Section 2.3.3. The limited number of data sources for sEVZ and Snæfellsnes means for these neovolcanic zones the error is calculated by Monte-Carlo simulation using quoted analytical uncertainties on data points. All regression parameters are calculated using York (1969).

increasing enrichment from north to south through the neovolcanic zones. This spatial pattern holds whether the mean or median ($\tilde{x}$) is calculated and is consistent with the inferences from the qq plots (Fig. 5). The systematic positive skew of the Pb isotopes from the NNVZ is also consistent with the deviations from normality recorded in Fig. 5.

The caution to the above analysis is that the moments reported in Table B.8 are all susceptible to sampling bias. Sample bias can easily arise where eruptions are not sampled, and their material not analysed, in proportion to their volume. Bias is especially likely to be a problem for the NNVZ, which has the smallest number of samples forming its distributions. The problem is compounded for the higher moments such as skewness for which it is not simple to estimate the uncertainty, making it difficult to quantify the significance of its deviations away from zero (Wright and Herrington, 2011). A more geological issue is in the way in which the distributions have been constructed. The most meaningful way of producing a univariate distribution would be to consider the volume of eruptions and elemental concentrations in weighting the distribution. This method would create kernel density estimates representing an isotopic budget of basalts and reduce sensitivity to sampling bias. However, much of the information required to make such calculations is missing from our database and it is beyond the scope of this study to supply it.

APPENDIX D. SPATIAL WEIGHTING FUNCTION

Throughout the paper we apply a Gaussian spatial weighting function, which scales according to the distance between points. For points i and j, the weighting takes the form,

$$w_{ij} = exp[-d_{ij}^2/(2b_i^2)], \quad \text{(D.1)}$$

where b_i is the bandwidth associated with the i^{th} point, and d_{ij} the distance between i and j. All distances have been calculated using the Vincenty inverse formula for ellipsoids, with the WGS84 parameters.

When calculating distances between spatially averaged parameters, an effective sample–sample distance is used instead of d_{ij} : $\hat{d}_{ij} = d_{ij}(1 - (w_{ij} + w_{ji})/2)$.

APPENDIX E. GLOBAL MORAN'S *I*

Moran's *I* is a measure of spatial autocorrelation, quantifying the similarity or dissimilarity of proximal points. The global version of Moran's *I* was introduced by Moran (1950). The expectation of *I* is,

$$E(I) = -1/(n-1) \quad \text{(E.1)}$$

An observed Moran's *I* greater than $E(I)$ indicates positive spatial autocorrelation, a Moran's *I* less than $E(I)$ indicates negative spatial autocorrelation.

In calculating the global Moran's *I* used in Table 6, the spatial weights matrix was constructed using a Gaussian weighting function with a bandwidth for each point that varied according to sample density. The initial bandwidth was set at 10 km, and then increased until at least 10 samples fell within a radius of one bandwidth. To avoid the effect multiple samples from single eruptions would have in increasing the spatial autocorrelation, a mean Pb–Sr–Nd isotopic composition has been calculated before determining *I*.

The signal to noise ratio of a geochemical signal will be an important control on the strength of spatial autocorrelation. The effect of this can be determined by degrading the signal of Pb isotopes to that of Sr and Nd isotopes. This is done by randomly re-sampling a Pb isotope ratio by its analytical uncertainty, scaled by the signal to noise ratio of the Pb isotope to that of the comparison isotope system. Degrading the Pb isotope signal for one thousand iterations and for each step calculating a Moran's *I* for the new dataset, allows calculation of an average *I* and a standard deviation. The results of this calculation for each of the Pb isotopes are given in Table 6.

APPENDIX F. GEOGRAPHICALLY WEIGHTED REGRESSION

Geographically weighted regression (GWR) is the combination of a weighted linear regression method with a spatial weighting function. There are multiple approaches to GWR (Fotheringham et al., 2002), but here we describe the specific implementation used in this paper, which uses the weighted least squares algorithm of York (1969).

The algorithm for calculating a map of local regression parameters is as follows:

1. A data point i is selected and the bandwidth of the spatial weights function is determined. Bandwidth starts at 10 km and increases in 1 km increments until at least 10 points are within one bandwidth of the central data point.
2. Weights are assigned to all data according to their distance from i, with spatially proximal points having a greater weight. Weights are calculated as described in Appendix D.
3. The vector of spatial weights is combined with weights determined from the analytical uncertainties on analyses (σ), so for a point j the total weight used in regression is $\omega_j = w_{ij}/\sigma_j^2$.
4. The linear regression method of York (1969) is used to calculate a gradient and intercept for the best fitting straight line. This method has the advantage of accounting for correlated error on both the x and y coordinates. The correlation coefficients for the error terms were calculated according to Albarède et al. (2004) Eq. 62.
5. The next data point is then stepped to, and the process repeated.

APPENDIX G. SUPPLEMENTARY DATA

Supplementary data associated with this article can be found, in the online version, at http://dx.doi.org/10.1016/j.gca.2013.08.032.

REFERENCES

Abouchami W., Galer S. J. G. and Hofmann A. W. (2000) High precision lead isotope systematics of lavas from the Hawaiian Scientific Drilling Project. *Chem. Geol.* **169**, 187–209.

Abouchami W., Hofmann A. W., Galer S. J. G., Frey F. A., Eisele J. and Feigenson M. (2005) Lead isotopes reveal bilateral asymmetry and vertical continuity in the Hawaiian mantle plume. *Nature* **434**, 851–856.

Agranier A., Blichert-Toft J., Graham D., Debaille V. and Albarède P. S. F. (2005) The spectra of isotopic heterogeneities along the Mid-Atlantic Ridge. *Earth Planet. Sci. Lett.* **238**, 96–109.

Albarède F., Télouk P., Blichert-Toft J., Boyet M., Agranier A. and Nelson B. (2004) Precise and accurate isotopic measurements using multiple-collector ICPMS. *Geochim. Cosmochim. Acta* **68**, 2725–2744.

Allègre C. J. (1982) Chemical geodynamics. *Tectonophysics* **81**, 109–132.

Allègre C. J., Hamelin B. and Dupré B. (1984) Statistical analysis of isotopic ratios in MORB: the mantle blob cluster model and the convective regime of the mantle. *Earth Planet. Sci. Lett.* **71**, 71–84.

Anselin L. (1995) Local indicators of spatial association – LISA. vol. 27. pp. 247–267.

Baker J., Peate D., Waight T. and Meyzen C. (2004) Pb isotopic analysis of standards and samples using a ^{207}Pb–^{204}Pb double spike and thallium to correct for mass bias with a double-focusing MC-ICP-MS. *Chem. Geol.* **211**, 275–303.

Ballmer M. D., Ito G., van Hunen J. and Tackley P. J. (2011) Spatial and temporal variability in Hawaiian hotspot volcanism induced by small-scale convection. *Nat. Geosci.* **4**, 457–460.

Barling J. and Weis D. (2008) Influence of non-spectral matrix effects on the accuracy of Pb isotope ratio measurement by MC-ICP-MS: implications for the external normalization method of instrumental mass bias correction. *J. Anal. At. Spectrom.* **23**, 1017–1025.

Bickle M. J., Bunbury J., Chapman H. J., Harris N. B. W., Fairchild I. J. and Ahmad T. (2003) Fluxes of Sr into the headwaters of the Ganges. *Geochim. Cosmochim. Acta* **67**, 2567–2584.

Björnsson A., Saemundsson K., Einarsson P., Tryggvason E. and Grönvold K. (1977) Current rifting episode in north Iceland. *Nature* **266**, 318–323.

Blichert-Toft J., Agranier A., Andres M., Kingsley R., Schilling J. G. and Albarède F. (2005) Geochemical segmentation of the mid-atlantic ridge north of Iceland and ridge-hot spot interaction in the north atlantic. *Geochem. Geophys. Geosyst.* **6**.

Brandon A. D., Graham D. W., Waight T. and Gautason B. (2007) ^{186}Os and ^{187}Os enrichments and high ^{3}He/^{4}He sources in the Earth's mantle: evidence from Icelandic picrites. *Geochim. Cosmochim. Acta* **71**, 4570–4591.

Breddam K. (2002) Kistufell: primitive melt from the Iceland mantle plume. *J. Petrol.* **43**, 345–373.

Breddam K., Kurz M. D. and Storey M. (2000) Mapping out the conduit of the Iceland mantle plume with helium isotopes. *Earth Planet. Sci. Lett.* **176**, 45–55.

Brooks C., Hart R. and Wendt I. (1972) Realistic use of two-error regression treatments as applied to rubidium–strontium data. *Rev. Geophy. Space Phys.* **10**, 551–577.

Chauvel C., Bureau S. and Poggi C. (2011) Comprehensive chemical and isotopic analyses of basalt and sediment reference materials. *Geostand. Geoanal. Res.* **35**, 125–143.

Chauvel C. and Hémond C. (2000) Melting of a complete section of recycled oceanic crust: trace element and Pb isotopic evidence from Iceland. *Geochem. Geophys. Geosyst.* **1**.

Collerson K. D., Kamber B. S. and Schoenberg R. (2002) Applications of accurate, high-precision Pb isotope ratio measurement by multi-collector ICP-MS. *Chem. Geol.* **188**, 64–83.

Debaille V., Tronnes R. G., Brandon A. D., Waight T. E., Graham D. W. and Lee C. T. A. (2009) Primitive off-rift basalts from Iceland and Jan Mayen: Os-isotopic evidence for a mantle source containing enriched subcontinental lithosphere. *Geochim. Cosmochim. Acta* **73**, 3423–3449.

DeMets C., Gordon R. G., Argus D. F. and Stein S. (1994) Effect of recent revisions to the geomagnetic reversal time scale on estimates of current plate motions. *Geophys. Res. Lett.* **21**, 2191–2194.

Douglass J. and Schilling J. G. (2000) Systematics of three-component, pseudo-binary mixing lines in 2D isotope ratio space representations and implications for mantle plume–ridge interaction. *Chem. Geol.* **163**, 1–23.

Dupré B. and Allègre C. (1983) Pb–Sr isotope variation in Indian Ocean basalts and mixing phenomena. *Nature* **303**, 142–146.

Elderfield H. and Greaves M. J. (1981) Strontium isotope geochemistry of Icelandic geothermal systems and implications for sea water chemistry. *Geochim. Cosmochim. Acta* **45**, 2201–2212.

Elliott T. R., Hawkesworth C. J. and Gronvöld K. (1991) Dynamic melting of the Iceland plume. *Nature* **351**, 201–206.

Ewart A., Collerson K. D., Regelous M., Wendt J. I. and Niu Y. (1998) Geochemical evolution within the Tonga–Kermadec–Lau arc-back-arc system: the role of varying mantle wedge compositions in space and time. *J. Petrol.* **39**, 331–368.

Fitton G. J., Saunders A. D., Kempton P. D. and Hardarson B. S. (2003) Does depleted mantle form an intrinsic part of the iceland plume? *Geochem. Geophys. Geosyst.* **4**.

Fitton G. J., Saunders A. D., Larsen L. M., Hardorson B. S. and Norry M. J. (1998) Volcanic rocks from the southeast Greenland margin at 63°N: composition, petrogenesis, and mantle sources. In *Proceedings of the Ocean Drilling Program, Scientific Results*, vol. 152 (eds. A. D. Saunders, H. C. Larsen and S. W. Wise). Ocean Drilling Program, College Station, TX, pp. 331–350.

Fotheringham A. S., Brunsdon C. and Charlton M. (2002) Geographically Weighted Regression: The Analysis of Spatially Varying Relationships. Wiley.

Galer S. J. G. and Abouchami W. (1998) Practical application of lead triple spiking for correction of instrumental mass discrimination. *Mineral. Mag.* **62A**, 491–492.

Green T. H., Sie S. H. and Cousens C. G. R. D. R. (1989) Proton microprobe-determined partitioning of Nb, Ta, Zr, Sr and Y between garnet, clinopyroxene and basaltic magma at high pressure and temperature. *Chem. Geol.* **74**, 201–216.

Halldorsson S. A., Oskarsson N., Grönovold K., Sigurdsson G., Sverrisdottir G. and Steinthorsson S. (2008) Isotopic-heterogeneity of the thjorsa lava – implications for mantle sources and crustal processes within the eastern rift zone, Iceland. *Chem. Geol.* **255**, 305–316.

Hanan B. B., Blichert-Toft J., Kingsley R. and Schilling J. G. (2000) Depleted Iceland mantle plume geochemical signature: artifact of multicomponent mixing? *Geochem. Geophys. Geosyst.* **1**.

Hanan B. B. and Schilling J. G. (1997) The dynamic evolution of the Iceland mantle plume: the lead isotope perspective. *Earth Planet. Sci. Lett.* **151**, 43–60.

Hart S. R. (1984) A large-scale isotope anomaly in the Southern Hemisphere mantle. *Nature* **309**, 753–757.

Hartley M. E. (2012) Postglacial volcanism and magmatism on the Askja volcanic system, North Iceland. Ph.D. thesis. The University of Edinburgh.

Hémond C., Arndt N., Litchenstein U., Hofmann A., Oskarsson N. and Steinthorsson S. (1993) The heterogeneous Iceland plume: Nd–Sr–O isotopes and trace element constraints. *J. Geophys. Res.* **98**, 15833–15850.

Hémond C., Condomines M., Fourcade S., Allègre C. J., Oskarsson N. and Javoy M. (1988) Thorium, strontium and oxygen isotopic geochemistry in recent tholeiites from Iceland: crustal influences on mantle-derived magmas. *Earth Planet. Sci. Lett.* **87**, 273–285.

Huang S., Hall P. S. and Jackson M. G. (2011) Geochemical zoning of volcanic chains associated with Pacific hotspots. *Nat. Geosci.* **4**, 874–878.

Ito G., Shen Y., Hirth G. and Wolfe C. J. (1999) Mantle flow, melting, and dehydration of the Iceland mantle plume. *Earth Planet. Sci. Lett.* **165**, 81–96.

Iwamori H. and Nakamura H. (2012) East–west mantle geochemical hemispheres constrained from Independent Component Analysis of basalt isotopic compositions. *Geochem. J.* **46**, e39–e46.

Jóhannesson H. and Smundsson K. (2009) Geological map of Iceland. 1:600 000. Tectonics (1st ed.). Icelandic Institute of Natural History, Reykjavik.

Jones S. M., White N., Clarke B., Rowley E. and Gallagher K. (2002) Present and past influence of the Iceland plume on sedimentation. *Geol. Soc. Lond. Spec. Publ.* **196**, 12–25.

Kamenov G. D., Mueller P. A. and Perfit M. R. (2004) Optimization of mixed Pb–Tl solutions for high precision isotopic analyses by ICP-MS. *J. Anal. At. Spectros.* **19**, 1262–1267.

Kelemen P. B., Hirth G., Shimizu N., Spiegelman M. and Dick H. J. B. (1997) A review of melt migration processes in the adiabatically upwelling mantle beneath oceanic spreading ridges. *Philos. Trans.: Math. Phys. Eng. Sci.* **355**, 283–318.

Kellogg L. H. and Turcotte D. L. (1987) Homogenisation of the mantle by convective mixing and diffusion. *Earth Planet. Sci. Lett.* **81**, 371–378.

Kellogg L. H. and Turcotte D. L. (1990) Mixing and the distribution of heterogeneities in a chaotically convecting mantle. *J. Geophys. Res.* **95**, 421–432.

Kempton P. D., Fitton J. G., Saunders A. D., Nowell G. M., Taylor R. N., Hardarson B. S. and Pearson G. (2000) The Iceland plume in space and time: a Sr–Nd–Pb–Hf study of the North Atlantic rifted margin. *Earth Planet. Sci. Lett.* **177**, 255–271.

Kitigawa H., Kobayashi K., Makishima A. and Nakamura E. (2008) Multiple pulses of the mantle plume: evidence from tertiary Icelandic lavas. *J. Petrol.* **49**, 1365–1396.

Kobayashi K., Tanaka R., Moriguti T., Shimizu K. and Nakamura E. (2004) Lithium, boron and lead isotope systematics of glass inclusions in olivines from Hawaiian lavas: evidence for recycled components in the Hawaiian plume. *Chem. Geol.* **212**, 143–161.

Kokfelt T., Hoernle K., Hauff F., Fiebig J., Werner R. and Garbe-Schönberg D. (2006) Combined trace element and Pb–Nd–Sr–O isotope evidence for recycled oceanic crust (upper and lower) in the Iceland mantle plume. *J. Petrol.* **47**, 1705–1749.

Kokfelt T. F., Hoernle K. and Hauff F. (2003) Upwelling and melting of the Iceland plume from radial variation of ^{238}U–^{230}Th disequilibria in postglacial volcanic rocks. *Earth Planet. Sci. Lett.* **214**, 167–186.

Kokfelt T. F., Hoernle K., Lundstrom C., Hauff F. and van den Bogaard C. (2009) Time-scales for magmatic differentiation at the Snaefellsjökull central volcano, western Iceland: constraints from U–Th–Pa–Ra disequilibrium in post-glacial lavas. *Geochim. Cosmochim. Acta* **73**, 1120–1144.

Koornneef J. M., Stracke A., Bourdon B. and Grönvold K. (2012a) The influence of source heterogeneity on the U–Th–Pa–Ra disequilibria in post-glacial tholeiites from Iceland. *Geochem. Cosmochim. Acta* **87**, 243–266.

Koornneef J. M., Stracke A., Bourdon B., Meier M. A., Jochum K. P., Stoll B. and Grönvold K. (2012b) Melting of a two-component source beneath Iceland. *J. Petrol.* **53**, 127–157.

Kuritani T., Yokoyama T., Kitagawa H., Kobayashi K. and Nakamura E. (2011) Geochemical evolution of historical lavas from Askja volcano, Iceland: implications for mechanisms and timescales of magmatic differentiation. *Geochim. Cosmochim. Acta* **75**, 570–587.

Lacasse C., Sigurdsson H., Carey S. N., Jóhannesson H., Thomas L. E. and Rogers N. W. (2007) Bimodal volcanism at the Katla subglacial caldera, Iceland: insight into the geochemistry and petrogenesis of rhyolitic magmas. *Bull. Volcanol.* **69**, 373–399.

Licciardi J. M., Kurz M. D. and Curtice J. M. (2007) Glacial and volcanic history of Icelandic table mountains from cosmogenic ^{3}He exposure ages. *Quat. Sci. Rev.* **26**, 1529–1546.

Maclennan J. (2008a) Lead isotope variability in olivine-hosted melt inclusions from Iceland. *Geochim. Cosmochim. Acta* **72**, 4159–4176.

Maclennan J. (2008b) Concurrent mixing and cooling of melts under Iceland. *J. Petrol.* **49**, 1931–1953.

Maclennan J., McKenzie D. and Grönvold K. (2001) Plume-driven upwelling under central Iceland. *Earth Planet. Sci. Lett.* **194**, 67–82.

Meibom A. and Anderson D. L. (2003) The statistical upper mantle assemblage. *Earth Planet. Sci. Lett.* **217**, 123–139.

Meyzen C. M., Blichert-Toft J., Ludden J. N., Humler E., Mével C. and Albarède F. (2007) Isotopic portrayal of the earth's upper mantle flow field. *Nature* **447**, 1069–1074.

Moran P. A. P. (1950) Notes on continuous stochastic phenomena. *Biometrika* **37**, 17–23.

Peate D. W., Baker J. A., Jakobsson S. P., Waight T. E., Kent A. J. R., Grassineau N. V. and Skovgaard A. C. (2009) Historic magmatism on the Reykjanes Peninsula, Iceland: a snap-shot of melt generation at a ridge segment. *Contrib. Miner. Petrol.* **157**, 359–382.

Peate D. W., Breddam K., Baker J. A., Kurz M. D., Barker A. K., Prestvik T., Grassineau N. and Skovgaard A. C. (2010) Compositional characteristics and spatial distribution of enriched Icelandic mantle components. *J. Petrol.* **51**, 1447–1475.

Press W. H., Teukolsky S. A., Vetterling W. T. and Flannery B. P. (). *Numerical Recipes in Fortran, 2nd ed.*. Cambridge University Press.

Rehkämper M. and Halliday A. N. (1998) Accuracy and long-term reproducibility of lead isotopic measurements by multiple-collector inductively coupled plasma mass spectrometry using an external method for correction of mass discrimination. *Int. J. Mass Spectrom.* **181**, 123–133.

Rehkämper M. and Mezger K. (2000) Investigation of matrix effects for Pb isotope ratio measurements by multiple collector ICP-MS: verification and application of optimized analytical protocols. *J. Anal. At. Spectrom.* **15**, 1451–1460.

Rickers F., Fitchner A. and Trampert J. (2013) The Iceland-Jan Mayen plume system and its impact on mantle dynamics in the North Atlantic region: evidence from full-waveform inversion. *Earth Planet. Sci. Lett.* **367**, 39–51.

Rudge J. F. (2008) Finding peaks in geochemical distributions: a re-examination of the helium-continental crust correlation. *Earth Planet. Sci. Lett.* **274**, 179–188.

Rudge J. F., Maclennan J. and Stracke A. (2013) The geochemical consequences of mixing melts from a heterogeneous mantle. *Geochim. Cosmochim. Acta* **114**, 112–143.

Rudnick R. L. and Goldstein S. L. (1990) The Pb isotopic compositions of lower crustal xenoliths and the evolution of lower crustal Pb. *Earth Planet. Sci. Lett.* **98**, 192–207.

Saal A. E., Hart S. R., Shimizu N., Hauri E. H. and Layne G. D. (1998) Pb isotopic variability in melt inclusions from oceanic island basalts, Polynesia. *Science* **282**, 1481–1484.

Schilling J. G., Kingsley R., Fontignie D., Poreda R. and Xue S. (1999) Dispersion of the Jan Mayen and Iceland mantle plumes in the Arctic: a He–Pb–Nd–Sr isotope tracer study of basalts from the Kolbeinsey, Mohns, and Knipovich ridges. *J. Geophys. Res. – Solid Earth* **104**, 10543–10569.

Shorttle O. and Maclennan J. (2011) Compositional trends of Icelandic basalts: implications for short-length scale lithological heterogeneity in mantle plumes. *Geochem. Geophys. Geosyst.* **12**.

Shorttle O., Maclennan J. and Jones S. M. (2010) Control of the symmetry of plume ridge interaction by spreading-ridge geometry. *Geochem. Geophys. Geosyst.* **11**.

Sigmarsson O., Condomines H. R. and Larsen H. (2000) The 1996 and 1998 subglacial eruptions beneath the Vatnajökull ice sheet in Iceland: contrasting geochemical and geophysical inferences on magma migration. *Bull. Volcanol.* **61**, 468–476.

Sigmarsson O., Condomines M. and Fourcade S. (1992) A detailed Th, Sr and O isotope study of hekla: differentiation processes in an Icelandic volcano. *Contrib. Miner. Petrol.* **112**, 20–34.

Sigvaldason G. E., Annertz K. and Nilsson M. (1992) Effect of glacier loading/deloading on volcanism: postglacial volcanic production rate of the Dyngjufjöll area, central Iceland. *Bull. Volcanol.* **54**, 385–392.

Silva I. G. N., Weis D., Barling J. and Scoates J. S. (2009) Leaching systematics and matrix elimination for the determination of high-precision Pb isotope compositions of ocean island basalts. *Geochem. Geophys. Geosyst.* **10**.

Skovgaard A. C., Storey M., Baker J., Blusztajn J. and Hart S. R. (2001) Osmium–oxygen isotopic evidence for a recycled and strongly depleted component in the Iceland mantle plume. *Earth Planet. Sci. Lett.* **194**, 259–275.

Sohn R. A. (2005) A general inversion for end-member ratios in binary mixing systems. *Geochem. Geophys. Geosyst.* **6**.

Steinthorsson S., Hardarson B. S., Ellam R. M. and Larsen G. (2000) Petrochemistry of the Gjálp-1996 subglacial eruption, Vatnajökull, SE Iceland. *J. Volcanol. Geotherm. Res.* **98**, 79–90.

Stracke A., Zindler A., Salters V. J. M., M^{c}Kenzie D., Blichert-Toft J., Albarède F. and Grönvold K. (2003) Theistareykir revisited. *Geochem. Geophys. Geosyst.* **4**.

Tanaka R., Makishima A. and Nakamura E. (2008) Hawaiian double volcanic chain triggered by an episodic involvement of recycled material: constraints from temporal Sr–Nd–Hf–Pb isotopic trend of the Loa-type volcanoes. *Earth Planet. Sci. Lett.* **265**, 450–465.

Tanaka T., Togashi S., Kamioka H., Amakawa H., Kagami H., Hamamoto T., Yuhara M., Orihashi Y., Yoneda S., Shimizu H., Kunimaru T., Takahashi K., Yanagi T., Nakano T., Fujimaki H., Shinjo R., Asahara Y., Tanimizu M. and Dragusanu C. (2000) JNdi-1: a neodymium isotopic reference in consistency with La Jolla neodymium. *Chem. Geol.* **168**, 279–281.

Thirlwall M. F. (1995) Generation of Pb isotopic characteristics of the Iceland plume. *J. Geol. Soc. Lond.* **152**, 991–996.

Thirlwall M. F., Gee M. A. M., Lowry D., Mattey D. P., Murton B. J. and Taylor R. N. (2006) Low $\delta^{18}O$ in the Icelandic mantle and its origins: evidence from Reykjanes Ridge and Icelandic lavas. *Geochim. Cosmochim. Acta* **70**, 993–1019.

Thirlwall M. F., Gee M. A. M., Taylor R. N. and Murton B. J. (2004) Mantle components in Iceland and adjacent ridges investigated using double-spike Pb isotope ratios. *Geochim. Cosmochim. Acta* **68**, 361–386.

Vance D. and Thirlwall M. (2002) An assessment of mass discrimination in MC-ICPMS. *Chem. Geol.* **185**, 227–240.

Weis D., Garcia M. O., Rhodes M., Jellinek M. and Scoates J. S. (2011) Role of the deep mantle in generating the compositional asymmetry of the Hawaiian mantle plume. *Nat. Geosci.* **4**, 831–838.

Welke H., Moorbath S., Cumming G. L. and Sigurdsson H. (1968) Lead isotope studies on igneous rocks from Iceland. *Earth Planet. Sci. Lett.* **4**, 221–231.

White W. M., Albarède F. and Télouk P. (2000) High-precision analysis of Pb isotope ratios by multi-collector ICP-MS. *Chem. Geol.* **167**, 257–270.

Woodhead J. D. (2002) A simple method for obtaining highly accurate Pb isotope data by MC-ICP-MS. *J. Anal. At. Spectrom.* **17**, 1381–1385.

Woodhead J. D. and Hergt J. M. (2000) Pb analyses of USGS reference materials. *Geostand. Newsl.* **24**, 33–38.

Wright D. B. and Herrington J. A. (2011) Problematic standard errors and confidence intervals for skewness and kurtosis. *Behav. Res.* **43**, 8–17.

York D. (1969) Least squares fitting of a straight line with correlated errors. *Earth Planet. Sci. Lett.* **5**, 320–324.

Zadnik M. G., Specht S. and Begemann F. (1989) Revised isotopic composition of terrestrial mercury. *Int. J. Mass Spectrom. Ion Processes* **89**, 103–110.

Associate edtitor: Janne Blichert-Toft